HAL
open science

SCA7 Mouse Cerebellar Pathology Reveals Preferential Downregulation of Key Purkinje Cell-Identity Genes and Shared Disease Signature with SCA1 and SCA2

Anna Niewiadomska-Cimicka, Frédéric Doussau, Jean-Baptiste Perot, Michel Roux, Celine Keime, Antoine Hache, Françoise Piguet, Ariana Novati, Chantal Weber, Binnaz Yalcin, et al.

To cite this version:

Anna Niewiadomska-Cimicka, Frédéric Doussau, Jean-Baptiste Perot, Michel Roux, Celine Keime, et al.. SCA7 Mouse Cerebellar Pathology Reveals Preferential Downregulation of Key Purkinje Cell-Identity Genes and Shared Disease Signature with SCA1 and SCA2. Journal of Neuroscience, 2021, 41 (22), pp.4910-4936. 10.1523/JNEUROSCI.1882-20.2021 . hal-03378998

HAL Id: hal-03378998

https://hal.science/hal-03378998v1

Submitted on 14 Oct 2021

HAL is a multi-disciplinary open access archive for the deposit and dissemination of scientific research documents, whether they are published or not. The documents may come from teaching and research institutions in France or abroad, or from public or private research centers.

L'archive ouverte pluridisciplinaire **HAL**, est destinée au dépôt et à la diffusion de documents scientifiques de niveau recherche, publiés ou non, émanant des établissements d'enseignement et de recherche français ou étrangers, des laboratoires publics ou privés.

Research Square

Preprints are preliminary reports that have not undergone peer review. They should not be considered conclusive, used to inform clinical practice, or referenced by the media as validated information.

SCA7 mouse cerebellar pathology reveals preferential downregulation of key Purkinje cell-identity genes and shared disease signature with SCA1 and SCA2.

Anna NIEWIADOMSKA-CIMICKA
Institut de Genetique et de Biologie Moleculaire et Cellulaire
Frédéric Doussau
CNRS UPR3212, Universite de Strasbourg
Jean-Baptiste Perot
Commissariat a l'energie atomique et aux energies alternatives Molecular Imaging Research Center
Michel J Roux
Institut de Genetique et de Biologie Moleculaire et Cellulaire
Céline Keime
Institut de Genetique et de Biologie Moleculaire et Cellulaire
Antoine Hache
Institut de Genetique et de Biologie Moleculaire et Cellulaire
Françoise Piguet
Institut de Genetique et de Biologie Moleculaire et Cellulaire
Ariana Novati
Universitatsklinikum Tubingen Institut fur Medizinische Genetik und angewandte Genomik
Chantal Weber
Institut de Genetique et de Biologie Moleculaire et Cellulaire
Binnaz Yalcin
Institut de Genetique et de Biologie Moleculaire et Cellulaire
Hamid Meziane
Institut Clinique de la Souris
Marie-France Champy
Institut clinique de la souris
Erwan Grandgirard
Institut de Genetique et de Biologie Moleculaire et Cellulaire
Alice Karam
Institut de Genetique et de Biologie Moleculaire et Cellulaire
Nadia Messaddeq
Institut de Genetique et de Biologie Moleculaire et Cellulaire

Aurélie Eisenmann
Institut de Genetique et de Biologie Moleculaire et Cellulaire
Emmanuel Brouillet
Commissariat a l'energie atomique et aux energies alternatives Molecular Imaging Research Center
Hoa Huu Phuc Nguyen
Institute of mecical Genetics and Applied Genomics, University of Tuebingen
Julien Flament
Commissariat a l'energie atomique et aux energies alternatives Molecular Imaging Research Center
Philippe Isope
CNRS UPR3212, Université de Strasbourg
Yvon Trottier (Yvon.Trottier@igbmc.fr)
Institut de Genetique et de Biologie Moleculaire et Cellulaire https://orcid.org/0000-0001-7230-4810

Research article

Keywords: Spinocerebellar ataxia type 7, Cell-type specific gene deregulation, Purkinje cells, Polyglutamine expansion, Cerebellum, Peripheral neuropathy, Retinopathy

Posted Date: July 23rd, 2020

DOI: https://doi.org/10.21203/rs.3.rs-27474/v2

License: This work is licensed under a Creative Commons Attribution 4.0 International License. Read Full License

---

Version of Record: A version of this preprint was published at The Journal of Neuroscience on April 22nd, 2021. See the published version at https://doi.org/10.1523/JNEUROSCI.1882-20.2021.

Abstract

Spinocerebellar ataxia type 7 (SCA7) is an inherited neurodegenerative disease mainly characterized by motor incoordination and visual impairment due to progressive cerebellar and retinal degeneration. Alteration of other nervous tissues also contributes to symptoms. The mechanisms underlying motor incoordination of SCA7 remain to be characterized. SCA7 is caused by a polyglutamine (polyQ) expansion in ATXN7, a member of the transcriptional coactivator SAGA complex, which harbors histone modification activities. PolyQ expansion in other proteins is responsible for 5 other SCAs (SCA1-3, 6 and 17). However, the converging and diverging pathophysiological points remain poorly understood. Using a new SCA7 knock-in model carrying 140 glutamines in ATXN7, we analyzed cell-type specific gene expression in the cerebellum. We show that gene deregulation affects all cerebellar cell types, although at variable degree, and correlates with alterations of SAGA-dependent epigenetic marks histone H3 acetylation and H2B ubiquitination. Our results further show that Purkinje cells (PCs) are far the most affected neurons: unlike other cerebellar cell types, PCs show reduced expression of 83 cell-type identity genes, critical for their spontaneous firing activity and synaptic functions. PC gene downregulation precedes morphological alterations, pacemaker dysfunction and motor incoordination. Strikingly, most PC identity genes downregulated in SCA7 mice are also decreased in early symptomatic SCA1 and SCA2 mice, revealing a common signature of early PC pathology involving cGMP-PKG and phosphatidylinositol signaling pathways and long-term depression. Our study thus points out molecular targets for therapeutic development which may prove beneficial for several SCAs. Finally, we show that unlike previous SCA7 mouse models, $SCA7^{140Q/5Q}$ mice exhibit the major disease features observed in patients, including cerebellar damage, cerebral atrophy, peripheral nerves pathology and photoreceptor dystrophy, which account for progressive impairment of behavior, motor and vision functions. Therefore, $SCA7^{140Q/5Q}$ mice represent an accurate model for the investigation of different aspects of SCA7 pathogenesis.

Introduction

Spinocerebellar ataxia type 7 (SCA7) is an adult-onset neurodegenerative disorder caused by a CAG repeat expansion in the *ATXN7* gene that is translated into an elongated polyglutamine (polyQ) tract in ATXN7 [1]. SCA7 expansions range from 37 to more than 200 repeats [2] and the length of the expanded repeats correlates inversely with the onset of symptoms and positively with disease severity and progression. Rare very large expansions ranging from 200-460 repeats cause infantile-onset SCA7, affect non-neural tissues and lead to early death [3-7]. ATXN7 is a subunit of Spt-Ada-Gcn5 Acetyltransferase (SAGA) [8], a multiprotein complex that regulates RNA polymerase II-dependent transcription through histone acetylation and deubiquitination activities.

The adult form of SCA7 is primarily characterized by the difficulty to coordinate balance, gait, and speech. Other common clinical features include spastic ataxia gait, dysphagia, intentional tremors, slow eye movements, ophthalmoplegia, as well as pyramidal signs [9, 10]. The pathology arises primarily from

progressive damage of the cerebellum and its associated tracts. Neuronal loss is observed in the Purkinje cell layer (PCL), the granule cell layer (GCL), the inferior olivary nuclei and the basis pontis associated with the atrophy of spinocerebellar and pyramidal tracts [9, 11-16]. Alteration of other structures including the telencephalon, midbrain and medulla oblongata is observed and may contribute to additional symptoms [10, 11, 17]. A peripheral neuropathy has been reported in some but not all neurophysiological studies [12, 18, 19]. A feature of SCA7, which differs from other inherited ataxias is the decrease of visual acuity due to loss of cone and rod photoreceptors [10, 12, 17, 20].

The visual impairment in SCA7 mouse models revealed a progressive loss of photoreceptor-specific gene expression, resulting in shortage of proteins necessary for renewal of outer segments, the highly dynamic photosensitive structure of terminally differentiated photoreceptors [2, 21-24]. Gene downregulation is due to dysfunction of GCN5-dependent acetylation activity of SAGA leading to histone hypoacetylation on photoreceptor gene promoters [25], and to alterations of the transactivation activity of cell-type specific transcription factors [21, 26, 27]. The results support the notion that ATXN7 mutation primarily alters the expression of photoreceptor identity genes and hence the maintenance of terminal neuronal differentiation [2]. Interestingly, zebrafish studies showed that Atxn7 is involved in the differentiation of photoreceptor and Purkinje cell (PC) during development [28, 29]. Whether PCs or other neurons also progressively lose their differentiation identity in SCA7 remains to be investigated.

In contrast to the retinopathy, the cellular and molecular mechanisms underlying SCA7 motor incoordination remain to be determined. Different transgenic mice showed different vulnerability of PCs to mutant ATXN7 (mATXN7) expression [30-36] and little overlap of cerebellar gene deregulation [32, 37, 38]. Interestingly, transgenic mice overexpressing mATXN7 in the whole brain except PCs or specifically in Bergmann glia developed motor dysfunction [33, 34], questioning the contribution of different cerebellar cell types to the pathology. However, the previous approaches have been insufficient to provide a deep understanding of the SCA7 cerebellar pathology at a single cell-type resolution.

Knock-in mouse models, in which a CAG repeat expansion is introduced in *Atxn7* show proper temporal and spatial expression of ATXN7 splicing isoforms and thus provide a genetically and physiologically more representative disease model. SCA7266Q/5Q knock-in mice show motor deficit and shrinkage of PC body size, but present a severe infantile-like pathology and early death, which limit the characterization of the motor phenotype [39]. A cognate SCA7100Q/5Q knock-in line develops late-onset pathology (half-life of ~19 months) and did not go through deep characterization [40]. Yet, the broad spectrum of SCA7 pathology has not been fully recapitulated in the current animal models. Furthermore, the contribution of SAGA dysfunction to cerebellar pathology is unclear as conditional deletion of GCN5 in mouse PCs led to very mild ataxia [40].

SCA7 is part of a group comprising 5 other SCAs (SCA1, SCA2, SCA3, SCA6 and SCA17) that are also caused by polyQ expansion in different gene products. PolyQ SCAs cause damage to the cerebellum, often with high vulnerability of PCs [41]. Despite shared genetic, clinical, and neuropathological features, more is needed to identify points of intersection and divergence of the pathophysiology of polyQ SCAs

[42]. While SCA proteins do not share any domain and have different cellular functions, changes in gene expression are central features in most polyQ SCAs. Therefore, the comparison of differentially expressed genes should provide insight into converging disease mechanisms.

To get insight into the mechanisms underlying motor incoordination and cerebellar degeneration, we used a new SCA7 knock-in mice line carrying 140 CAG repeats. A comprehensive and longitudinal characterization of this model using a battery of analyses (motor and behavioral tests, retina imaging, MRI, electrophysiology, neuropathology) indicates that SCA7140Q/5Q mice remarkably recapitulate the major clinical features observed in patients, including cerebellar damage, specific cerebral atrophy, peripheral nerves pathology and photoreceptor dystrophy, which account for progressive impairment of behavior, motor and vision functions. Using this relevant model, we developed a methodology to analyze cell-type specific gene expression in the cerebellum and determined the morphological, electrophysiological and gene expression features of the most vulnerable neurons, the PCs. Our study further show that both SAGA-dependent epigenetic marks - histone H3 acetylation and H2B deubiquitination - are altered and correlate with gene deregulation. Finally, in contrast to other cerebellar cell types, PCs show a profound downregulation of neuronal identity genes, which are also downregulated in other polyQ SCAs. Thus, our study uncovers a signature of PC identity genes highly vulnerable to polyQ expansion mutation, revealing a converging pathomechanisms in polyQ SCAs.

Methods

Mouse information.

The SCA7$^{140Q/5Q}$ knock-in mouse line, which is derived from the SCA7$^{266Q/5Q}$ mouse model [39] by CAG repeat contraction, harbors an expansion ranging from 140-150 CAG repeats in exon1 of the *Atxn7* locus. Mice are kept on C57Bl/6J background and bred in the Mouse Clinical Institute (Illkirch, France) with a 12 h light/dark cycle and free access to food and water. Genotyping was performed by PCR as described previously [39]. Wild type (WT) and SCA7$^{140Q/5Q}$ males and females were analyzed, unless indicated.

Behavioral and motor performance analysis.

To ensure the replicability of SCA7 mouse phenotype, two mouse colonies were raised in the husbandry of different research centers and were analyzed using standardized protocols by independent experimenters and instruments. The experiments were all performed during the light phase of a 12h light/dark cycle.

Open field test. The open fields were placed in a room homogeneously illuminated at 150 lux. Mice of the first colony were tested in automated open fields (44.3 x 44.3 x 16.8 cm, Panlab, Barcelona, Spain), virtually divided into central and peripheral regions. Each mouse was placed in the periphery of the open field and allowed to explore freely for 30 min, with the experimenter out of the animal's sight. The distance traveled, the number of rears, average speeds and resting time were automatically recorded and reflect the general locomotor or motor activity phenotype. The number of entries and the time spent in the central and peripheral regions were used as index of emotionality/anxiety. Mice of the second colony were tested in an open field (46 x 46 cm). Each mouse was tracked over 30 minutes with EthoVision XT 11 and 12 (Noldus Information Technology, The Netherlands) and automatically analyzed for the same parameters, except for the number of rears that were manually scored.

Rotarod. To assess the ability to maintain balance, mice of the first colony were tested on a rotating rod of 5 cm in diameter covered by grey rubber foam (Bioseb, Chaville, France). Mice were given three testing trials during which the rotation speed accelerated from 4 to 40 rpm in 5 min. Trials were separated by a minimum of 5-10 min interval. The average latency before falling from the rod was used as index of motor coordination performance. Mice of the second colony were assessed using an apparatus from TSE Systems (Bad Homburg, Germany) with 3.5 cm rod diameter without rubber foam, using the same parameters as for the first colony. The floor of the rotarod was covered with soft material to avoid animal discomfort when falling. Light intensity was set to about 115 lux.

Notched bar. The test was used to test hindlimb coordination. On the first day, mice were trained on a 2 cm-wide and 110 cm long natural wooden notched bar made of 26 platforms of 2 cm long spaced by 27 gaps of 2 cm and connected to the goal box (12 x12 x 14 cm), under 115 lux. The second day mice were tested in the same conditions and time to cross the notched bar was measured. A back paw going through a gap was considered as an error.

Beam walking test. The test consisted of a 110 cm long wooden beam (2 cm diameter), positioned 50 cm above the floor. One extremity of the beam was used as starting position while the opposite extremity was connected to a goal box (of 12 x12 x 14 cm for the first colony, and 8.5 x 8.5 x 12 cm for the second colony). The floor of the goal boxes was covered with clean sawdust. The floor under the beam was covered with soft material. During the whole protocol, the light intensity in proximity of the beam was maintained at about 115 Lux. Each mouse was first habituated to the goal box for 1 minute

before three training and three testing trials. On the first training trial, mice were placed on the beam near and facing the goal box and allowed to access it. On the second and third training trials, mice were placed further away (33- and 66-cm, respectively) facing the box and were allowed to reach and enter the box. On the testing sections, mice were placed at the beam extremity (100 cm, starting position), facing the box and were allowed to reach the goal box. After each training and testing trial, mice were left for 15 seconds in the goal box. The latency to reach the box (cut off 60 seconds) and the number of errors (slips) while crossing the beam were recorded.

Footprint. After coating the front- and hind feet with 2 different colors of non-toxic inks, mice walked through a tunnel (length: 50 cm, width: 9 cm, height: 6 cm) covered with paper. The following five footprint patterns were manually measured: matching between paws, stride length, stance width, distance between fore- and hindlimbs.

Grip strength test. This test measures the maximal muscle strength (g) using an isometric dynamometer connected to a grid (Bioseb). Mice were held by the tail and allowed to grip the metal grid with the 4 paws, then they were pulled backwards until they released it. Each mouse was submitted to 3 consecutive trials and the maximal strength developed by the mouse before releasing the grid was recorded. The average value of the three trials adjusted to body weight was used as index of the muscle strength.

CatWalk. Gait analyses were performed using CatWalk XT 8.1 (Noldus Information Technology, Wageningen, The Netherlands). The CatWalk apparatus consists of a closed corridor resting on a glass plate. The walkway (20 cm) is illuminated with red light from the ceiling and green light from the edges of the plate (green intensity threshold: 0.30; camera gain: 20). When an animal enters the corridor, the light reflected by the paws is detected by a camera placed 25 cm below the walkway. Each mouse was placed on the walkway at one extremity and allowed to move in the corridor in both directions. Only runs lasting a maximum of 10 seconds with 60% maximal speed variation were counted. Five successful runs per animal were recorded. The swing (s) defined as the duration of no contact of a paw with the glass plate was analyzed separately for fore- and hindlimbs and averaged between left and right sides.

Optical Coherence Tomography and electroretinography.

Optical Coherence Tomography (OCT). Pupils were dilated with a bilateral topical application of atropine (1%, Virbac, France). Animals were then anesthetized using isoflurane (4% for induction, 2% for maintenance in a 2 l.min-1 flow of 50-50% mix of air and O_2) and placed on the stage of a Bioptigen R2200 spectral domain OCT (Bioptigen, North Carolina, USA). Cornea was kept moisturized with a thin layer of ocular gel (Ocry-gel, TVM, France) applied with surgical eye spears. For each eye, a rectangular scan was obtained, corresponding to a region of 1.4 x 1.4 mm centered on the optic nerve. The thicknesses of the whole retina (including the pigmentary epithelium), the segments, the outer nuclear layer, the inner nuclear layer and the inner plexiform layer for a given eye were calculated as the average of 2 measures performed manually at 0.5 mm from the optic nerve center using the Bioptigen InVivoVue 2.4.33 software.

Electroretinography (ERG). Pupils were dilated and cornea moisturized as described above. Mice were then anesthetized with an intraperitoneal injection of a mixture of ketamine (100 mg/kg) and medetomidine (1.2 mg/kg, Domitor®, Vétoquinol, France). Mice were placed on a platform on top of a chemical heating pad (Aquapack, China). A DTL thread was used as the active electrode and placed across the cornea. To minimize invasiveness, we replaced the subcutaneous needles traditionally used as reference and ground electrodes, respectively by a gold loop placed in the mouth (around the incisors), and a finger clip electrode placed on the tail with conductive paste. The platform was then moved forward to position the mouse head inside a Ganzfeld with flashes controlled with a Visiosystem (SIEM Bio-médicale, Nice, France). The background light was set at 25 $Cd.m^{-2}$. Single flash photopic responses were recorded for intensities of 1, 3 and 10 $Cd.s.m^{-2}$, and flicker responses were recorded at frequencies of 2, 5, 10, 20 and 25 Hz with 3 $Cd.s.m^{-2}$ flashes. The b-wave amplitude was measured offline with the Visiosystem software. At the end of the test, mice received a subcutaneous injection of atipamezole (10 mg/kg, Antisedan®, Vétoquinol, France) to counteract the action of medetomidine, and were placed on a heating plate set at 37°C until awakening.

Electrophysiology.

Electromyography. Recordings were performed using the Natus UltraProS100 apparatus (Mag2Health, France). Mice were anesthetized using intraperitoneal injection with ketamine/xylazine (130/13mg/kg). Animals were maintained at 37°C during the whole experiment until wake up. Latency and amplitude of

M and H waves were recorded in the plantar hind paw muscle after sciatic nerve stimulation (0.1 ms and 8 mA intensity).

Electrophysiology of PCs. Following anesthesia by isoflurane inhalation, cerebellum extraction was done in ice-cold (~1°C) artificial cerebrospinal fluid (ACSF) bubbled with carbogen (95% O_2, 5% CO_2) containing (in mM): 120 NaCl, 3 KCl, 26 NaHCO3, 1.25 NaH_2PO_4, 2.5 $CaCl_2$, 2 $MgCl_2$, 10 D-glucose and 0.05 mM minocyclin. Cerebella were sectioned (Microm HM650V, Germany) in an ice-cold low- sodium and zero-calcium slicing buffer containing (in mM): 93 *N*-Methyl-D-Glucamine, 2.5 KCl, 0.5 CaCl2, 10 MgSO4, 1.2 NaH2PO4, 30 NaHCO3, 20 HEPES, 3 Na-Pyruvate, 2 Thiourea, 5 Na-ascorbate, 25 D-glucose and 1 Kynurenic acid. Sagittal slices 300 µm thick were immediately transferred in bubbled ACSF for 30 minutes at 34°C and maintained at room temperature (~25°C) in bubbled ACSF for at least 1 hour before transfer in a recording chamber, continuously perfused with bubbled ACSF. In order to block inhibitory and excitatory synaptic transmission, blockers of $GABA_A$-receptors (100µM picrotoxin) and ionotropic glutamate receptors (1 mM kynurenic acid) were added in ACSF. PCs located in lobules VI or IX/X were visually identified under infrared illumination. All recordings were performed at near physiological temperature (32 ± 0.5°C) using an AxoPatch 200A (Molecular Devices, USA). PC discharges were monitored using extracellular recordings with pipettes filled with 0.5 M NaCl (resistance: 15–30 MW). Data were acquired using WinWCP 4.5.4 freeware (John Dempster, University of Strathclyde, Glasgow, UK; RRID:SCR_014713). Recordings were sampled at 50 kHz and filtered at 2 kHz. In extracellular recordings, action potentials were detected using OpenElectrophy, an open source software (http://neuralensemble.org/OpenElectrophy/; RRID:SCR_000819) (Garcia and Fourcaud- Trocme´, 2009). Data were stored in SQL databases (Oracle). Spike trains were analyzed using Python software written in-house (SynaptiQs developed by Antoine Valera) and custom-based routines. discharge irregularity was assessed by two parameters: (1) the mean of interspike intervals (ISIs); (2) coefficient of variation for adjacent ISIs (CV2) calculated as follows:

$$CV_2 = 2\frac{|ISI_{n+1} - ISI_n|}{|ISI_{n+1} + ISI_n|}$$

where ISI_n and ISI_{n+1} are two consecutive ISI. An average of CV2 over all consecutive pairs of ISI's estimates the intrinsic variability of PC pacemaking activity. This parameter is independent of slow

variations in the firing pattern.

Neuroanatomical study.

Neuroanatomical study was carried out using 10 mice at 33 weeks (n=5 per group) and 12 mice at 50 weeks (n=6 per group). Brain samples were fixed in 4% buffered formalin for 48 hours. Seventy-eight brain parameters, made of area and length measurements, were taken blind to the genotype across three coronal sections as described [43]. Data were analyzed using a t-test with equal variances to determine whether a brain region is associated with neuroanatomical defect or not.

Magnetic resonance imaging (MRI).

After paraformaldehyde (PFA) perfusion of 25-week-old mice, brains were removed and stained for one week in a solution of Gadolinium (Dotarem©, Guerbet, France) in PBS at 2.5 mM. This protocol enhances the signal- and contrast-to-noise ratios on MR images of fixed brains [44], *Ex vivo* MRI experiments were performed on a horizontal 11.7 T Bruker scanner (Bruker, Ettlingen, Germany). A quadrature cryoprobe (Bruker, Ettlingen, Germany) was used for radiofrequency transmission and reception. High-resolution anatomical images were acquired using Echo Planar Imaging sequence (Resolution= 100x100x200 μm^3, TR= 3000 ms, TE= 28 ms). In order to preserve integrity to avoid deformations, brains were kept inside skulls for *ex vivo* MRI experiments. Anatomical images were co-registered in the same space to create a study template. Transformations to match the study template to an atlas composed of a high-resolution template and a map of region's labels adapted from the Allen mouse brain Atlas [45] were calculated. Finally, transformations to match the study template and labels to each individual anatomic image were calculated. The automated segmentation pipeline was performed using an in-house python library (Sammba-MRI, https://github.com/sammba-mri/sammba-mri).

Immunofluorescence.

Cryosections. Mice were transcardialy perfused with 1xPBS followed by 4% PFA/1xPBS. Brains and eyecups were immediately dissected and incubated in 4% PFA/1xPBS overnight (o/n) or for 2h, respectively. They were washed 3 times in 1xPBS before a 24h incubation in 30% sucrose for cryoprotection and then mounted in Shandon Cryomatrix embedding resin (ThermoFisher) and

immediately frozen. 14-20 µm brain sagittal and 12 µm eyecup cryosections (Leica CM 3050S) were collected and stored at -80°C.

Vibratome sections. Brains were fixed as described above, washed 3 times in 1xPBS and mounted in 2% agarose/1xPBS. Vibratome sagittal sections (Leica VT 1000S) of 50 µm were collected, washed in 1xPBS, next in 20% glycerol/1xPBS and stored in 60% glycerol/1xPBS at -20°C. The 60% glycerol/1xPBS was washed out with 1 wash of 20% glycerol/PBS and 3 washes of 1xPBS before immunofluorescence.

Cryosections were permeabilized in PBSTx (1xPBS/0.1 % Triton X-100) and blocked for 1h at room temperature (RT) with PBSTx supplemented with 7% deactivated fetal calf serum (FCS). Sections were incubated o/n at 4°C with primary antibodies in a blocking buffer using the following dilutions: 1:20 000 (cryosections) or 1:5 000 (floating sections) anti-CALB1 (rabbit, D28k, Swant, CB38a); 1:5 000 (cryosection) or 1:1 000 (floating section) anti-CALB1 (mouse, D28k, Sigma, C9848); 1:1 000 (floating sections) vGLUT2 (Guinea Pig, Merck, AB2251-I); 1:1 000 anti-ATXN7 (rabbit, 1261; IGBMC); 1:700 anti-GFAP (mouse, Sigma, G3893). Secondary goat anti-rabbit, goat anti-mouse, goat anti-guinea pig IgG antibodies (ThermoFisher, dilution 1:1000) conjugated with Alexa 555, Alexa 488 and Alexa 488 fluorophores, respectively, were applied for 1h at RT and subsequently washed 3 times in PBSTx. Nuclei were counterstained with 1 µg/ml DAPI (4',6-diamidino-2-phenylindole dihydrochloride). Controls without primary antibodies were performed in parallel. Slides were mounted with Aqua Poly Mount (Polysciences), dried and stored at +4°C protected from light.

Floating cerebellar sections were processed as described above with the following modifications. Sections were incubated in Eppendorf tubes for 3 days at 4°C with primary antibodies in 300 µl of blocking buffer. Secondary antibodies were applied for 2h at RT. Sections were positioned on slides directly before mounting.

Retina images were acquired on a Leica DM 4000B with a Cool SNAP HQ2 camera with 40x objective with zoom factor 2.5 and processed with Fiji. Cerebellum images were acquired either on a confocal microscope (SP8, Leica) with 40x/1.3 oil objective with a zoom factor 1 or on a Spinning disc with Leica DMI 8 inverted microscope equipped with Hamamatsu Orca flash 4.0 Camera 5 (Gataca Sytem) connected with Metamorph software (Molecular Devices). For the acquisitions, HC PL APO 40x/1.3 oil objective and three diode lasers (405, 488, and 561 nm) were used. Image brightness and contrast were equivalently adjusted in Fiji for display purposes when necessary.

PC size and circularity measurements.

Sagittal floating sections (50 µm) of central vermis were immunostained with anti-Calbindin1 antibody and acquired using confocal SP8 (Leica) microscope. The obtained z-stacks were subdivided into 3 groups of 15 slices using Fiji. After background subtraction the PC layer was outlined manually in the vicinity of PC somas. Next, a customized Fiji macro allowing an automatic detection and measurement the PC area and circularity was applied. The macro was kindly provided by Stephane Collins (Inserm UMR1231 GAD, Dijon, France). Manuel correction was performed dendritic parts were identified as PC. Edge PC were excluded from measurements.

Morphometry of cerebellar vermis sections.

Sagittal 20 µm sections of central vermis were immunostained with anti-CALB1 antibody and counterstained with DAPI. Sections were scanned with Digital Slide Scanner Nanozoomer 2.0 HT (Hamamatsu) using 40x magnification. Images of the cerebellum were visualized using NDPI viewer and exported with 5x magnification into tiff format. Length and width of cerebellar sections as well as the thickness of the molecular cell layer were measured using Fiji software.

vGLUT2 density, volume and extension in the molecular cell layer.

Sagittal floating sections (50 µm) of central vermis were immunostained with anti-Calbindin1 and anti- vGLUT2 antibodies, counterstained with DAPI. Sections were acquired using YoKogawa CSU W1 Spinning disc with Leica DMI 8 inverted microscope and Hamamatsu Orca flash 4.0 Camera (Gataca Sytem) and a driver by the Metamorph software (Molecular Devices). For the acquisitions, HC PL APO 40x/1.3 oil objective and three diode lasers (405, 488, and 561 nm) were used. Stacks consisted of 225 z-slices with 0.2 µm z-step using 6.5 µm x 6.5 µm pixel size.

Images were saved in tiff format. Subsequently, RGB channels were split in Fiji. Channel with vGLUT2 acquisition («.ims» format) was exported to Imaris v 9.3.1 (Bitplane AG) for 3D reconstruction. The region of interest, namely the molecular cell layer, was selected and 3D volumes were created with the surface module of Imaris. Next, vGLUT2 was analyzed only on this region with the Imaris spot module. The detection of objects in 3-dimensional space was based on both intensity and size (with the estimated XY diameter of 1µm). Only spots ranging from 0.52 to 30 μm^3 were selected to eliminate

background. Density and volume measurements of spots were analyzed in Excel and GraphPad Prism 6. The extension of vGLUT2-positive climbing fiber terminals along the dendrites of PC was measured using Fiji. Namely, the ratio of the extension of the 3D reconstructed vGLUT2 spots in the molecular cell layer over the total length of the molecular cell layer was calculated for the central part of lobule VI and for the side part of lobule X.

Histology and electron microscopy analysis.

Eyes were prepared for histology and electron microscopy as in [24]. Semi-thin (2 µm) sagittal sections were cut with an ultramicrotome (Leica Ultracut UCT) and stained with toluidine blue, and histologically analyzed by light microscopy. For sciatic nerve preparation, animals were perfused with 5 mL of PBS and 10 mL 4% PFA in saline, and tissues were fixed in 2.5% PFA/2.5% glutaraldehyde in cacodylate buffer. Ultra-thin (70 nm) sections were cut and contrasted with uranyl acetate and lead citrate and examined at 70kv with a Morgagni 268D electron microscope. Images were captured digitally by Mega View III camera (Soft Imaging System) and contrast was adjusted for display purposes.

Western blot analysis.

Cerebellum and retina were dissected and snap frozen in liquid nitrogen. Their whole cell extracts were obtained by lysis and sonication of the tissue in, respectively, 500 µl and 150 µl of the buffer containing 50mM Hepes-KOH (pH 7.5), 140mM NaCl, 1mM EDTA, 0.1% Na-deoxycholate, 1% SDS, 1% Triton-X100, 1x Protease Inhibitor Cocktail (Roche), 20mM N-ethylmaleide, 20mM nicotinamide. The last two compounds were not used for ATXN7 detection. Protein concentrations were measured using Bradford protein assay. 10 µg (histone analysis) and 30 µg (ATXN7 analysis) of total proteins were used for electrophoresis. Electrophoresis was run in 4-12% Bis-Tris Protein Gels in NuPAGE MOPS SDS Running Buffer (ThermoFisher) for histone analysis and in NuPAGE™ 3-8% Tris-Acetate

Protein Gels in NuPAGE™ Tris-Acetate SDS Running Buffer (ThermoFisher) for ATXN7 detection. Following electrophoresis, proteins were transferred on nitrocellulose membrane for 1.5 h at 200 mA or overnight at 30mA. Antibodies were diluted in 1x PBSTM (1xPBS with 0.1% Tween, and 5% non-fat

milk). The following primary antibodies were applied overnight at 4°C: anti-ATXN7, 1:1 000 (ThermoFisher, PA1-749); anti-H2B, 1:10 000 (IGBMC clone H2-2A8); anti-H2Bub 1:2 000 (MediMabs, MM-0029); anti-H3K9ac 1:2 000 (Abcam ab4441); anti-GAPDH 1:10 000 (Merck Millipore, MAB374); anti-TUBB 1:2 000 (IGBMC, 2A2). Secondary antibodies: Peroxidase AffiniPure F(ab')□ Fragment Goat Anti-Rabbit IgG (H+L) (GARPO; 1:10 000, Jackson ImmunoResearch Lab.) and Peroxidase AffiniPure Goat Anti-Mouse IgG (H+L) (GAMPO; 1:10 000, Jackson ImmunoResearch Lab.) were applied in 1x PBSTM for 2h at RT, washed three times in 1xPBST, and proteins were detected using SuperSignal West Pico PLUS Chemiluminescent kit (ThermoFisher). Chemiluminescent signal was acquired on Amersham Imager 600. Images were analyzed using Fiji.

RNA-seq library preparation and sequencing.

RNA-Seq libraries were prepared from 300 ng of total RNA using TruSeq Stranded mRNA Library Prep Kit and TruSeq RNA Single Indexes kits A and B (Illumina, San Diego, CA), according to manufacturer's instructions. Briefly, following purification with poly-T oligo attached magnetic beads, mRNA were fragmented using divalent cations at 94°C for 2 minutes. RNA fragments were reverse transcribed into first strand cDNA using random primers. Strand specificity was achieved by replacing dTTP with dUTP for the second strand cDNA synthesis using DNA Polymerase I and RNase H. Following addition of a single 'A' base and subsequent ligation of the adapter on double stranded cDNA fragments, products were purified and amplified by PCR (30 sec at 98°C; [10 sec at 98°C, 30 sec at 60°C, 30 sec at 72°C] x 12 cycles; 5 min at 72°C) to create the cDNA library. Surplus PCR primers and adapter dimers were removed by purification using AMPure XP beads (Beckman-Coulter, Villepinte, France) and the final cDNA libraries were checked for quality and quantified using capillary electrophoresis. Libraries were sequenced on Illumina Hiseq 4000 sequencer as Single-Read 50 base reads following Illumina's instructions. Image analysis and base calling were performed using RTA 2.7.3 and bcl2fastq 2.17.1.14. Adapter dimer reads were removed using DimerRemover (https://sourceforge.net/projects/dimerremover/)

RNA-seq data analysis.

Image analysis and base calling were performed using RTA 2.7.3 and bcl2fastq 2.17.1.14. Reads were mapped onto the mm10 assembly of mouse genome using Tophat v2.0.14 [46] with bowtie v2.1.0 aligner. Gene expression was quantified using HTSeq v0.6.1 [47] and gene annotations from Ensembl

release 86. Statistical analysis was performed using R and DESeq2 v1.6.3 Bioconductor library [48]. Gene functional annotations were performed using Ingenuity Pathway Analysis (IPA) and String v10.5 software [49, 50].

Analysis of public datasets.

For SCA1 dataset (GEO: GSE75778), FASTQ files were retrieved from Sequence Read Archive using fastq-dump (SRA Toolkit v2.8.0, BioProject PRJNA305316, samples: GSM1967518- GSM1967520; GSM1967524- GSM1967529; GSM1967533 - GSM1967538; GSM1967542 - GSM1967544), and only the first 50 bases of read 1 sequences were retained for further analysis. For SCA2 dataset (Array Express: E-MTAB-6293), FASTQ files were retrieved from Sequence Read Archive using fastq-dump (SRA Toolkit v2.8.0, BioProject PRJEB24319, samples ERR2237861- ERR2237880, ERR2237882 - ERR2237893). Reads were then mapped onto the mm10 assembly of mouse genome using Tophat v2.0.14 [46] with bowtie v2.1.0 aligner. Gene expression was quantified using HTSeq v0.6.1 [47] and gene annotations from Ensembl release 90. Statistical analysis was performed using R and DESeq2 v1.18.1 [48].

Microarray probe sets of Doyle et al. [51] were converted into gene names according to mm10 annotation using the Affymetrix NetAffx Annotation File (Mouse430_2 Annotations, Release 36). Next, the cell-type subdivided datasets were curated to indicate the genes present uniquely in one cell-type dataset and in more than 1 cell-type datasets. The obtained gene lists were used to study cell-type distribution of transcriptional changes in SCA7.

Quantitative RT-PCR.

Total RNA samples were extracted from 1 cerebellum/sample or 2 retinas/animal/sample using TriReagent (MRC) following the manufacturer's instruction. 500ng of purified RNA was then reverse transcribed using QuantiTect® Reverse Transcription kit (Qiagen) according to the manufacturer's protocol. The real-time qPCR (RT-qPCR) reactions were performed on obtained cDNAs (1/20 dilution) using QuantiTect SYBR Green PCR Master Mix (Qiagen), and specific primers (Table S1) with a Light Cycler 480 (Roche). Gene expressions were normalized based on the expression of *Hprt or 36B4 (Rplp0)*.

Statistical analysis.

Information on number (n) values and what n represents (e.g., animals, biological replicates) and definition of center and dispersion and precision measures [e.g., mean, median, standard error of the

mean (SEM)] can be found in figure legends. Data were analyzed using GraphPad Prism 7 or 8 or Stat view. Differences between means were assessed with unpaired Student's *t* test, one-way analysis of variance (ANOVA) or ordinary two-way ANOVA or two-way ANOVA with repeated measurement, followed by post-hoc testing of pairwise comparisons among genotypes, (Bonferroni correction), as indicated. Differences between median were analyzed using Mann-Whitney test. Survival of mice with different genotype and sex was plotted using the Kaplan-Meier method and statistical comparisons were performed using the Log Mantel-Cox test. Further information are indicated in figure legends and in Table S2. Significance was established at $p < 0.05$. Data are expressed as mean ± SEM unless indicated.

Results

General phenotypic features of SCA7 mice carrying 140 CAG repeats.

SCA7140Q/5Q heterozygous mice have a median lifespan of 54 weeks for both males and females (Fig 1a). SCA7140Q/140Q homozygous mice have a much shorter lifespan than heterozygotes. Age-related body weight increase of SCA7140Q/5Q and SCA7140Q/140Q mice significantly differed from their WT littermates (males $F(11,220)=105$, $p < 0.0001$; females $F(11,242)=36,1$, $p < 0.0001$). SCA7140Q/5Q females and males gained weight at the same rate as WT mice up to 12 and 14 weeks, respectively, and then plateaued until 24 weeks with an underweight of 18% for females and 20% for males compared to WT of the same sex and age (Fig 1b). Subsequently, the weight of SCA7140Q/5Q decreased, while remaining stable for WT mice. The body weight of SCA7140Q/140Q mice plateaued earlier at 10 weeks for males and 12 weeks for females, and strongly decreased after 20 weeks. Compared to age-matched WT male and female littermates, the body lengths of adult SCA7140Q/5Q and SCA7140Q/140Q males were significantly shorter by 6.6% ($p < 0.01$) and 23% ($p < 0.0001$), respectively, and those of adult SCA7140Q/5Q and SCA7140Q/140Q females by 6.5% ($p < 0.05$) and 21% ($p < 0.0001$), respectively (Fig 1c). SCA7140Q/5Q mice, which represent the genetic status of most SCA7 patients, were used for a detailed phenotypic characterization.

Examination of general physical appearance and body shape of SCA7140Q/5Q mice did not reveal gross morphological abnormalities at 28 weeks of age. The proportion of lean, fat and bone tissues was similar to their WT littermates, when normalizing to body weight (S1 Fig). From about 40 weeks of age, SCA7140Q/5Q mice showed already severe motor deficit and were easily distinguishable from control animals due to their smaller body size and hypoactivity, and some with a hunched posture (kyphosis) and tremors. Because of the poor health status and following recommendation of our animal health regulator, SCA7140Q/5Q mice were generally sacrificed at this stage.

Degeneration of photoreceptors, pigmented epithelium and Bruch's membrane.

Previous studies of SCA7 mouse retinopathy mainly focused on photoreceptor pathology. To get a broader insight into the SCA7140Q/5Q mouse retinopathy, longitudinal analysis was made by correlating non-invasive OCT and ERG, and histological and molecular analysis. The OCT measurement of 8 different morphological parameters indicated that the overall structure of SCA7140Q/5Q retina was normal at 9 weeks (Fig 2a-c and S2 Fig). However, from 15 weeks, photoreceptor segment layers progressively got thinner with age as compared to WT littermates (Fig 2b). The same was observed for the outer nuclear layer (ONL) but occurred later (23 weeks) and not as severely (Fig 2c). There was no clear scalable alteration of thickness of the inner nuclear layer (INL), the inner plexiform layer (IPL) or any other eye structures in SCA7 mice, except for the anterior chamber that showed a significant reduction from 23 weeks onward (S2 Fig).

ERG studies in SCA7 patients showed that cone dysfunction precedes rod dysfunction [17]. We evaluated cone function of WT and SCA7140Q/5Q mice by measuring the cone-derived b-wave amplitudes of photopic (single flashes ERG of 1, 3 and 10 Cd.s.m-2) and flicker responses (5 frequencies between 2 and 25 Hz) over time. At 5 weeks, b-wave amplitudes of both photopic and flicker responses of SCA7140Q/5Q mice were similar to WT littermates. However, at 10 weeks, the b-wave amplitudes of photopic and flicker responses of SCA7140Q/5Q mice significantly decreased relative to WT mice, between 32% and 36% for photopic flashes and between 37% and 45% depending on flicker frequency (Fig 2d- e and S3 Table). The loss of b-wave amplitudes of photopic responses and flicker further worsened with age, with reductions between 81% and 100% at 23 weeks.

The green and blue opsin (OPN1MW, OPN1SW, respectively) of cones and the rhodopsin (RHO) of rods are light-sensitive pigments that initiate vision and represent major components of photoreceptor outer segments. RT-qPCR showed that expression of these photoreceptor identity genes progressively decreased with age in SCA7140Q/5Q mice (Fig 2f). Notably, the level of *Opn1mw* and *Opn1sw* RNAs already showed about 65% ($p < 0.01$) and 90% ($p < 0.01$) reduction, respectively, in 10-week-old mutant mice, when cone-derived ERG responses began to decrease. The decrease of cone opsin RNAs was earlier and more drastic than for the *Rho* RNA, consistent with the primary alteration of cone function in SCA7 patients. Therefore, the loss of cone ERG of SCA7140Q/5Q mice closely correlates with the loss of cone opsins expression, as shown in previous SCA7 mouse models, and both occur before a significant shortening of outer segments detected by OCT.

Histology and electron microscopy indicated that photoreceptor outer segments are almost completely lost at 44 weeks in SCA7140Q/5Q mice and at 20 weeks in SCA7140Q/140Q mice, while inner segments showed only a slight reduction in both SCA7 genotypes, compared to WT retina (Fig 2g and S2i-k Fig). Additional degenerative signs of SCA7 photoreceptors included disorganization of the remnant outer segments, swollen mitochondria and vesicular membrane accumulation in inner segments, several dark stained inner segments and photoreceptor nuclei (Fig 2h-k). Interestingly, we found striking anomalies of

the retinal pigmented epithelium (RPE) and Bruch's membrane of SCA7140Q/5Q retina, never reported in previous models to our knowledge. Firstly, the thickness of RPE was clearly increased in SCA7 mice as compared to controls (Fig 2l). Secondly, on electron microscopy, while the normal RPE (Fig 2m) contains translucent infolding membranes in contact all along the basement membrane, SCA7 RPE showed discontinuous and opaque infolding membranes, with homogenous deposits between the plasma membrane and the basement membrane (Fig 2n, The Bruch's membrane of SCA7 retina showed enlargement and disorganization, as compared to WT in which the Bruch's membrane was thin and regular (Fig 2m-o).

Deficits in motor activity and coordination.

We performed longitudinal motor performance analysis of SCA7140Q/5Q and WT male littermates using a variety of motor activity paradigms. The spontaneous activity measured with the open field showed that SCA7140Q/5Q mice become significantly hypoactive at 16 weeks, and hypoactivity worsened with age (Fig 3a-d). Specifically, they travelled shorter distances in the arena, ran slower, rested longer times, and made less rears than WT littermates. However, SCA7140Q/5Q mice did not show anxiety behavior, since they explored the central area similarly to WT mice (Fig 3e).

When comparing the mean latency to fall from the accelerated rotarod, SCA7140Q/5Q mice fell earlier than WT mice with statistically significant differences from the age of 24 weeks (Fig 3f). On the notched bar test, SCA7140Q/5Q mice performed similarly to WT littermates up to 17 weeks (Fig 3g, h). From 20 weeks, performance worsened relative to age-matched WT mice for the time required and the number of mistakes done when crossing the bar. For beam walking test, SCA7140Q/5Q mice took longer time to cross the bar from 20 weeks (Fig 3i), while the number of mistakes was not significantly different between genotype (data not shown).

The forward gait patterns were quantitatively assessed for spatial and temporal gait parameters, both for the fore- and hind-limbs, using respectively footprint and Catwalk, an automated gait analysis system. On footprint, SCA7 and WT mice performed similarly in all gait parameters until 17 weeks. From 21 weeks, SCA7140Q/5Q mice made significantly shorter steps (stride length) with forelimbs and hindlimbs of each body side (Fig 3j). Similarly, the stance width between forelimbs or between hindlimbs was consistently shorter in SCA7140Q/5Q mice from 21 weeks (Fig 3k). Temporal gait analysis as recorded by Catwalk showed that the swing duration of right and left forelimbs were significantly affected in SCA7140Q/5Q mice from 25 weeks, while the swing duration of hindlimbs were not affected (Fig 3l,m). Finally, the grip strength test showed that the muscle strength of SCA7140Q/5Q mice normalized to animal body weight was similar to WT mice (Fig 3n).

Replicability of mouse phenotyping across laboratories has important implications in fundamental research and preclinical studies and is often hampered by methodological issues. To assess the replicability of SCA7 mouse phenotype, a second SCA7140Q/5Q mouse colony was raised in the husbandry of a different research center and was analyzed by independent experimenters and

instruments. Mice from the second colony were tested using the standardized protocols established for the first colony (see Methods for further details). As in the first colony, SCA7140Q/5Q males gained less weight than WT littermates, reaching a plateau at 14 weeks (S3a Fig). However, the average weights of adult SCA7140Q/5Q and WT males from the second colony were 6.5% ($p < 0.0001$) lighter than the mice of the first colony (S3b Fig), indicating a significant environment effect regardless of the genotype. As for the first colony, open field analysis revealed the hypoactivity of SCA7140Q/5Q mice from 16 weeks of age, with a decreased total distance travelled in the arena, a decreased average speed, an increased resting time and a decreased number of rears (S3c-f Fig). In contrast to the first colony, the exploration of the open central area (S3g Fig) suggested a tendency of SCA7 mice to anxiety behavior in the second environment. As for the first colony, SCA7140Q/5Q mice of the second colony took significantly longer time to cross the beam walking bar (S3h Fig). However, accelerated rotarod, which had a smaller rod diameter than the previous apparatus used for the first colony, led to short latency to fall even for WT at baseline and hence did not reveal any difference in the latency between the two genotypes (S3i Fig).

In summary, the hypoactivity of SCA7140Q/5Q mice revealed by open field tests appeared at an early time point (onset at 16 weeks), while defects in motor performances (as shown in rotarod of the first colony) and in specific proprioceptive abilities (as reflected by gait alteration in notched bar, beam walking, footprint and catwalk) appeared later between 20-25 weeks, depending of the test. Except for rotarod, the onset and progression of motor phenotypes of SCA7140Q/5Q were replicable in two different research centers.

Morphological and functional alterations of the peripheral nervous system.

A peripheral neuropathy was reported in some but not all neurophysiological studies in patients [12, 18, 19] and has never been explored in mouse models. To understand the cause of motor alterations in SCA7140Q/5Q mice, the activity of the peripheral nervous system was first assessed over time by measuring the sciatic nerve function by electromyography. At 15 weeks, median amplitudes of plantar M-wave and H-wave of SCA7140Q/5Q mice were similar to WT littermates (Fig 4a-b). However, both plantar M-wave and H-wave amplitudes were reduced by 21% ($p < 0.05$) and by 33% ($p < 0.05$), respectively, at 32 weeks in SCA7 mice. At 43 weeks, the plantar M-wave amplitude was reduced by 31% ($p < 0.05$), while the H-wave was almost absent (95%, $p < 0.0001$). To correlate these functional abnormalities with structural status, sciatic nerve sections were analyzed by histology and electron microscopy. Compared to WT mice, cross section of sciatic nerve of SCA7 mice showed clear alterations of myelinated fibers and decreased number of small fibers (Fig 4c). On electron microscopy (Fig 4d-o), several structural alterations were observed in myelinated fibers of SCA7140Q/5Q mice, including myelin degeneration and infolding-like structures as well as axonal modifications characterized by inner swelling tongue and autophagy. Non-myelinated fibers displayed abnormal structures of Remak bundles. In conclusion, motor components of the sciatic nerve morphology and activity are affected in SCA7140Q/5Q mice.

Distinct morphological alterations in SCA7 mouse brain.

Brains of SCA7 patients show prominent neurodegeneration in the cerebellum and atrophy of other brain regions. To establish a systematic survey of brain damage of SCA7 mice, the morphology of three different coronal brain sections of SCA7140Q/5Q and WT mice was studied using neuroanatomical measurement of 78 anatomy parameters across 20 distinct brain subregions [43]. At 33 weeks, there was no major surface difference between SCA7140Q/5Q mice and WT littermates. However, end-stage SCA7140Q/5Q mice (50 weeks) showed significant reduction of brain areas in the three coronal sections (from -6.7% to -8%) with both white and grey matter alterations (S4 Fig). Atrophy of grey matter structures included the somatosensory cortex, the pons, while affected white matter regions comprised the corpus callosum, the anterior commissure, the internal capsule and the fimbria of the hippocampus. We then aimed to capture SCA7 mouse brain alterations at earlier disease stage using high resolution MRI. MRI measurement clearly showed a global atrophy of the SCA7 mouse brains compared to WT at 25 weeks ($p < 0.05$) (Fig 5a). Moreover, the decrease of whole brain volume of SCA7140Q/140Q mice was two times higher than SCA7140Q/5Q ($p < 0.05$), confirming the stronger severity of the disease in homozygous mice. Interestingly, our automated segmentation pipeline highlighted specific brain regions particularly atrophied in the mouse model such as the corpus callosum, and subparts of the hippocampus and cortex (Fig 5b and S5 Fig). No significant atrophy of the cerebellar cortex was measured in SCA7 mice, which can be due to strong variability of volume measurement in this structure. To further correlate cerebellar neuropathology and motor alterations, morphometric parameters were measured on sagittal sections of the central vermis at different disease stages (Fig 5c-g). The vermis length (axis from lobule V to IX) of SCA7140Q/5Q mice was smaller to WT at 34 weeks (Fig 5c). Interestingly, the vermis width (axis from lobule VI to X) was significantly shorter in SCA7140Q/5Q mice at 12 weeks already and this difference remained at later stages but did not worsen with the motor phenotype (Fig 5d). Strikingly, there was no major or progressive alteration of the molecular cell layer (MCL) thickness in any of the lobules analyzed (Fig 5f, g and data not shown).

Morphological and functional alterations of Purkinje cells.

Since PCs are highly vulnerable neurons in inherited ataxias, their morphology, connectivity and function were investigated. The area of PC soma was significantly smaller in lobule VI ($p < 0.002$) of 34- week SCA7140Q/5Q compared to age-matched WT mice, while in lobules IX and X PC soma did not differ (Fig 6a-e). In contrast, PC circularity index was affected in lobules IX and X ($p < 0.006$ and $p < 0.0005$, respectively), but not in lobule VI (Fig 6f-h). We then analyzed synapses integrity between PC and climbing fibers (CF) of inferior olivary neurons. To this purpose, we quantified vGLUT2-immunolabeling of CF-PC contact points in the MCL. The average density and average volume of vGLUT2 contact points were similar in WT and SCA7 mice (data not shown). However, extension of climbing fiber terminals along the PC dendritic tree was significantly reduced in lobule VI and X by 15.8% ($p=0.029$) and 23% ($p=0.034$), respectively, in SCA7140Q/5Q compared to WT mice (Fig 6i, j). Moreover, co-immunolabeling of vGLUT2 and CALB1 revealed frequent aggregation of vGLUT2 contact points along large dendritic

arborization of PC in SCA7 cerebellum (Fig 6k). Therefore, despite different morphological alterations of PC soma of lobule VI and X, synaptic contacts between PC and CF were affected in both lobules.

Intrinsic membrane properties of PC determine their spontaneous firing pattern even in the absence of synaptic inputs [52, 53]. Any alteration in the precision of their pacemaking activity may be the result of PC cellular dysfunctions and may affect cerebellar functions [54]. To investigate the correlation between PC function, morphological phenotypes and motor deficits, we assessed whether the intrinsic properties of PC spontaneous discharge were altered in SCA7140Q/5Q mice at 22 and 38 weeks. We recorded spontaneous activity of PC located in lobule VI and IX/X in WT and SCA7 littermates using juxtacellular recordings of PC in acute cerebellar slices at a near physiological temperature (32°C) (Fig 6l). To focus on PC intrinsic excitability and to rule out network contributions, excitatory and inhibitory synaptic transmissions were pharmacologically blocked. PC discharges were evaluated using the mean firing frequency (measurement of the mean ISI) and the CV2, which estimates the variability of the firing pattern between two consecutive ISIs [55, 56]. At 22 weeks, no difference in the firing properties of PCs located in lobule VI was detected between WT and SCA7 mice. In contrast, in symptomatic SCA7 mice of 38 weeks, PC exhibited a higher regularity of discharge in both lobules VI ($p < 0.001$) and IX/X ($p < 0.001$) (Fig 6m,n) and a decrease in the mean firing rate in lobule VI ($p = 0.004$) (Fig 6o). Our results show that intrinsic properties of PC excitability are altered in symptomatic SCA7 mice.

Accumulation of mutant ATXN7 in retina and cerebellum.

Previous studies showed that mATXN7 tends to misfold and form intracellular protein aggregates (reviewed in [2]). To determine the dynamic of mATXN7 aggregation in SCA7 mice we performed immunofluorescence and western blot analysis of retina and cerebellar sections. In WT retina and cerebellum, ATXN7 immunolabeling is barely detectable (S6a,b Fig). In contrast, the immunolabeling progressively increased with age in SCA7 mouse tissues, indicating that mATXN7 accumulates over time. This resulted in different labeling profiles depending of the neuronal population. mATXN7 aggregates were readily detected in many photoreceptor nuclei at 12 weeks, became widespread in all retinal neuron nuclei at later stages. In SCA7 cerebellum, PCs showed the earliest mATXN7 accumulation that progressively increased between 12 and 19 weeks, leading to the formation of large nuclear aggregates at later stages. mATXN7 nuclear aggregates were also observed in the MCL and GCL. All cerebellar lobules showed the accumulation of mATXN7 in PC nuclei (S6c Fig).

Western blot analysis showed the expression of normal ATXN7 as a 110 kilodalton (kDa) band in control retina and cerebellar samples (S6d Fig). In SCA7 samples, the mutant form of ATXN7 migrated at ~140 kDa. From 5-8 weeks of age, mATXN7 was also detected as high molecular weight smear in these tissues, indicating that mATXN7 accumulates as insoluble oligomeric forms, much before the formation of visible nuclear aggregates as detected by immunolabeling of tissues.

Cerebellar gene expression changes in SCA7 mice.

To gain molecular insight into the cerebellar dysfunctions of SCA7140Q/5Q mice, gene expression profiles of cerebellar samples of symptomatic SCA7 mice and their WT littermates were analyzed by RNA-seq. Analysis of differentially expressed genes indicated that 406 genes are downregulated in SCA7 cerebella and 270 genes are upregulated ($p < 0.05$) (Fig 7a). Ingenuity Pathway Analysis (IPA)

[50] of the 676 differentially expressed genes revealed that the most significantly affected functions ($p \leq 0.0002$) concern major neuronal signaling pathways involving glutamate, G-protein coupled receptors, calcium, CREB and cAMP, and LTD (Fig 7b and S4 Table), most of which have previously been implicated in the pathogenesis of other ataxias [54].

IPA also pointed out the impairment of interferon signaling pathway (Fig 7b). Interestingly, among the 10 most predicted upstream regulators ($p \leq 7*10-9$) of the differentially expressed genes, 8 are implicated in the modulation of interferons signaling pathways (Table S5). Moreover, functional annotations of the 270 upregulated genes using STRING [49] further highlighted a strong enrichment (false discovery rate (FDR) $<2*10-6$) of type 1 interferon pathway (S7 Fig). The interferon regulator factor 7 gene (*Irf7*), which is the second most significantly upregulated protein-coding gene (2.7 fold; $p = 2.28*10-10$) in SCA7 mouse cerebella, composed with high confidence (0.700) a protein-protein association network of 19 direct edges that includes signal transducer and activator of transcription 1 (*Stat1*), which further interconnects with the proto-oncogene *Jun*. Together, *Irf7*, *Stat1* and *Jun* constituted the center a large network of 189 edges involving multiple upregulated genes coding for proteins involved in immune system response (S7 Fig), further emphasizing the important activation of interferon signaling pathway in SCA7 cerebella. Chort et al. [57] previously reported the increased level of interferon-beta and its receptor in the cerebellum of the SCA7266Q/5Q model. Our transcriptome data provide additional evidence of the activation of a regulatory network involving interferon signaling.

Downregulation of a large subset of Purkinje cell identity genes.

To gain insight into the cell type-specific distribution of differentially expressed genes in SCA7 cerebella, we took advantage of the publicly available actively translated mRNA profiles of all the major cerebellar cell types [51]. To compare with our SCA7 RNA-seq dataset, the published datasets [51] were reannotated using Affymetrix microarray probesets annotations on mm10 genome assembly. This reannotation led to a total of 9671 actively translated transcripts in the different cell types of WT cerebellum (S8 Fig). 89% of them were present in the SCA7 dataset. Out of 9671 actively translated transcripts, we identified 5058 transcripts assigned to only one of the nine major cerebellar cell type datasets, including 801 transcripts in PC, 2357 in granule cells, 156 in Golgi cells, 340 in stellate and basket cells, 144 in unipolar brush cells, 563 in oligodendrocytes expressing Olig2, 133 in oligodendrocytes expressing Cmtm5, 279 in Bergmann glia and 285 in astrocytes (S8 Fig and S6 Table). Taking the cellular distribution into account, we were able to determine the cell-type specificity of 470 differentially expressed genes of SCA7 cerebellum and found that 240 of them were assigned to a single cerebellar cell type and 230 were present in more than one cell type (Table S7). The analysis revealed that all the cerebellar cell types presented differentially

expressed genes (Fig 7c,d), indicating that SCA7 pathology is widespread across cerebellar cell types. However, despite the rarity of PC in the cerebellum estimated to 0.1% of cerebellar cells, 23% (106 out of 470) of SCA7 deregulated genes were assigned to PC. In contrast, 15% of SCA7 deregulated genes were assigned to granule cells, while this cell type represents 90% of cerebellar cells. Importantly, while granule cell genes were both up- and downregulated, almost all PC genes (104 out of 106 genes) were downregulated (Fig 7d), indicating that repression of PC genes is a major component of SCA7 cerebellar pathology. Another publicly available datasets from Kratz et al. [58] allowed us to identify 5 additional PC genes that were downregulated in SCA7 mouse cerebella (Table S7), resulting in a total 109 downregulated PC genes.

To ascertain the specificity of these 109 genes in PC, their pattern of expression was analyzed using *in situ* hybridization datasets reported in The Brain Transcriptome Database (BrainTx; CDT) [59] and in the Allen Brain Atlas [45]. We established three categories of genes according to the level of enriched expression in PC, as specifically expressed in PC compared to other cerebellar cells, enriched in PC or non-enriched in PC (e.g. equally present in other cell types). The analysis showed that 83 genes had specific enrichment in PC, and are thus considered as PC identity genes that showed reduced expression in SCA7 mice. The remaining genes were expressed in wider range of cerebellar cell types or were not present in *in situ* hybridization datasets and were then excluded from further analysis (Table S8).

RT-qPCR was used to study the time course of repression of a subset of PC identity genes in SCA7140Q/5Q cerebella. The *Grid2*, *Calb1*, *Fam21* and *Rora* genes showed decreased expression in SCA7 mice from 27 weeks, coinciding with the onset of motor alterations (S9 Fig). Interestingly, the 3 PC genes *Pcp4*, *Fam107b and Rgs8* showed downregulation already at 12 weeks, a pre-symptomatic stage of the disease, suggesting a strong implication in PC pathology of SCA7 mice.

A signature of downregulated PC identity genes in SCA1, SCA2 and SCA7.

To further explore whether PC genes downregulated in SCA7 have pathological relevance in cerebellar ataxia, we looked at publicly available transcriptomic datasets of SCA1 and SCA2 mouse models in which the mutant genes were specifically expressed in PC and caused spontaneous firing dysfunction [60, 61]. In these 2 models, expression level of a subset genes was also shown to be altered compared to their respective WT littermates [60, 61]. Before proceeding with the comparative analysis, we have reanalyzed the RNA-seq raw data of SCA1 mouse cerebella at 5, 12 and 28 weeks and SCA2 cerebella at 6 weeks with the same software which was used for SCA7. We then compared the differentially expressed genes in the cerebellum of the three SCA models. The analysis revealed that 136 genes common to the 3 datasets were downregulated and only 5 were upregulated (Fig 7e,f). Interestingly, out of the 136 downregulated genes, 67 were PC identity genes including 10 genes previously associated with genetic ataxias (Table 1 and Table S9). These 67 genes were downregulated already at 5 weeks in SCA1 and at 6 weeks in SCA2 mice, which are disease onset stages of these models [61, 62], and

constitute a signature of early pathological processes of PC. The comparison performed with the SCA1 dataset at later disease stages revealed 13 additional downregulated PC identity genes in common with SCA2 and SCA7 mice (Table 1), suggesting that these 13 genes were associated with the progression of PC pathology.

The biological significance of the early downregulation of the 67 PC identity genes was researched using 3 analyses. First, the KEGG pathway analysis indicated that this set was enriched for genes involved in LTD (FDR 0.0036), cGMP-PKG signaling pathway (FDR 0.0068) and phosphatidylinositol signaling system (FDR 0.0069) (Fig 7g). Second, the STRING analysis [49] was used to search for functional partnerships and interactions between proteins encoded by the 67 PC genes. It revealed a network of 45 edges (p value = 1.2e-13) (Fig 7g) interconnecting a large number of proteins encoded by genes showing mutations in human or mouse model ataxias, such as *Grid2*, *Calb1*, *Car8*, *Trpc3*, *Kcnma1*, *Inpp5a*, *Inpp4a*. The network also showed central positions to the regulator of G-protein signaling 8 (RGS8), phospholipase C beta 3 (PLCB3) and cGMP-dependent kinase PRKG1, the latter two are related to LTD and synapse functions of PC [54, 63]. Finally, our list of 67 PC identity genes was compared to a published list of genes composing the SCA1 Magenta gene module [61]. This module was established using the WGCNA (Weighted Gene Coexpression Network Analysis) of SCA1 cerebellar transcriptomes and reported to be enriched in PC genes involved in LTD and glutamate signaling and to be of high relevance for SCA1 pathogenesis [61]. We found that 48 out of 67 PC- enriched genes were present in the Magenta module. Furthermore, two major hub genes described in the module, namely *Fam107b* and *Rgs8,* were within the top strongest downregulated genes in SCA1, SCA2 and SCA7 models, and were already downregulated at 12 weeks in SCA7 mice, hence before onset of motor symptoms (S9 Fig). Altogether, these analyses suggest that the dysfunction of synaptic LTD of PC constitutes a common pathway in the early pathogenesis of SCA1, SCA2 and SCA7.

Finally, to identify mechanisms which could account for the downregulation of the 67 PC identity genes, we first looked at RORa (RAR-related orphan receptor alpha), a key transcription factor involved in PC differentiation and survival [64] and showing downregulation in SCA1, SCA2 and SCA7 mice (Table 1). Among the 67 PC genes, 19 genes were known RORa-target genes [64, 65] (Table 1), suggesting that RORa dysfunction accounts for PC genes deregulation. We then performed *in silico* analysis of 2-kb promoter sequence of the 67 PC genes to search for *de novo* motifs and transcription factors binding sites using MEME, TOMTOM, AME or FIMO [66]. The analysis did not reveal major enrichment of other transcription factor binding motifs in the promoter of the 67 PC identity genes affected, compared to control sequences (e.g. shuffled promoter sequences or promoter sequences of

67 PC-enriched non-deregulated genes) (data not shown). Deregulation of gene expression may depend on alteration of diverse processes including chromatin structure, nucleosomal occupancy and histone modifications, which play important roles in transcriptional regulation. Given the presence of ATXN7 in the histone-modifying SAGA complex, we determined whether the bulk level of histone marks regulated by SAGA were altered in SCA7 cerebellum. The level of H2Bub was significantly increased in SCA7140Q/5Q cerebellum compared to WT, while the level of H3K9ac showed no significant difference

(Fig 8a,b). However, a significant decrease of H3K9ac was observed in SCA7140Q/140Q homozygous mice, which were more severely affected that the SCA7 heterozygous mice (S10 Fig). Together, this suggests that mutant ATXN7 differentially alters the histone-modifying activities of SAGA complex along the progression of cerebellar pathology and could impact on transcription of cerebellar genes.

Discussion

SCA7 is a devastating neurological disease affecting primarily the cerebellum and retina, and no treatment can currently prevent or slow down the disease process. Accurate models of the disease are required as confident tools for a better understanding of SCA7 pathogenesis and for developing therapeutic strategies. In this study, we used a new and highly relevant mouse model to determine the molecular and cellular basis of the cerebellar pathology of SCA7. By combing cerebellar gene profiling and single-cell-type resolution as well as morphological and functional studies, PCs came out as the most affected cerebellar cell type and showed profound loss of expression of neuronal identity genes, critical for their spontaneous firing and synaptic functions. These observations suggest disease mechanisms primarily altering the maintenance of PC differentiation, and are consistent with similar pathological features described for SCA7 mouse photoreceptors in this and earlier studies. Like in SCA7 mice, PC identity genes were also affected in pre-symptomatic SCA1 and SCA2 mice, indicating convergence of pathomechanisms underlying PC vulnerability in these polyQ SCAs.

Retinal, PNS and CNS features of SCA7 mice.

Unlike previous mouse models, the SCA7140Q/5Q line combines most cardinal disease features observed in adult SCA7 patients, including retinal, cerebral, cerebellar and peripheral nerve pathologies. Symptoms develop and progress in a suitable time window for preclinical trials and can be quantitatively evaluated using a series of robust motor, functional, histological and molecular parameters (S11 Fig). In contrast to the severely affected mouse line, SCA7140Q/5Q mice present no complication related to husbandry, as male fertility and offspring delivery are normal.

The SCA7140Q/5Q line recapitulates photoreceptor degenerative features as observed in earlier mouse models [2, 21, 22, 30, 39]. In normal retinal, photoreceptor function is maintained by sustained expression of photoreceptor identity genes essential to the daily renewal of outer segments, a structure entirely filled with discs of folded double membranes where phototransduction takes place. In SCA7140Q/5Q retina, photoreceptor dysfunction correlates with the progressive reduced expression of photoreceptor identity genes such as opsin genes and the disappearance of outer segments as shown by OCT and electron microscopy. In zebrafish, knock-down of *atxn7* impedes the formation of photoreceptor outer segments during development of the eye [28, 29]. Together, this suggests that mATXN7 toxicity alters a normal function of ATXN7 in the maintenance of outer segments, a cell-type specific structure characteristic of photoreceptor terminal differentiation [67]. SCA7140Q/5Q shows alterations in the RPE and Bruch's membrane, also reported in patients [12]. These observations warrant further investigation as the

interaction between photoreceptor and RPE is essential for proper visual function. Interestingly, the homogenous deposits observed between RPE plasma membrane and basement membrane of SCA7140Q/5Q mice, resemble sub-RPE deposits reported in Malattia Leventinese mouse model [68], a dominantly inherited macular degenerative disease. These mice bears a mutation in Efemp1, a proposed interactor of ATXN7 [69].

Peripheral pathologies account for the neurological phenotype in SCA7140Q/5Q mice. Electromyograph studies revealed that motor peripheral activities are reduced at 32 weeks, due to lesions of myelin and myelinated fibers of sciatic nerve. The sensory component might also be affected as non-myelinated fibers also show alterations. SCA7140Q/5Q mice findings parallel the most recent study of SCA7 patients, who showed abnormal motor and sensory nerve conductions [18], and complement previous neuropathological evidence of degenerating signs in the dorsal root and anterior horn of patients' spinal cord [12, 14].

Post mortem brains showed atrophy and neuronal loss in diverse brain regions, which could account for a variety of neurological symptoms present in adult-onset SCA7 patients [11, 12]. SCA7140Q/5Q mice also present significant decreased volume of selected brain regions at 24 weeks. Interestingly, MRI analysis shows atrophy of the corpus callosum, hippocampus and cortical regions, which parallels observations of human SCA7 [12, 70]. In particular, recent studies showed altered functional connectivity between patients' cerebellum and hippocampus or parahippocampal areas that may account for specific memory dysfunctions [15, 71-73]. The hippocampus is a brain region where mutant ATXN7 rapidly accumulates in SCA7140Q/5Q (data not shown) and in SCA7266Q/5Q mice [39]. In the latter model, mATXN7 accumulation was correlated to specific alteration of the short-term synaptic plasticity of hippocampal neurons [39]. The cerebellar cortex showed no significant atrophy, which can be due to strong variability of volume measurement by MRI in this structure. Indeed, in our *ex vivo* imaging setup, the cerebellum was peripheral in the field of view, where the magnetic field was less homogeneous and coil sensitivity was lower. Direct morphometric analysis of SCA7 cerebellar sections showed that the vermis width is slightly but significantly smaller before the onset of the motor symptoms. At end-disease stage (52 weeks), SCA7140Q/5Q brain showed additional atrophy of the pons and somatosensory cortex as well as the anterior commissure, the internal capsule and the fimbria of the hippocampus. Overall, brain alterations in the SCA7140Q/5Q mice recapitulate many characteristics of human SCA7.

PC pathology of SCA7 mice.

Previous analysis of the cerebellar pathology in SCA7 lacked single-cell resolution of functional and molecular alterations. Our study of SCA7140Q/5Q mice indicates that PCs show morphological alterations of soma and synapses, impairment of spontaneous firing, and early and progressive repression of PC genes involved in firing and synaptic functions.

It is well known that precision of PC pacemaking activity is essential for normal cerebellar functions and any impairment of PC intrinsic excitability leads to ataxic behaviors [54]. In several rodent models of

ataxia, PCs are characterized by a lower rate of spontaneous firing compared to WT and/or by an irregular firing pattern [54, 62, 74-76]. Here, we show that PCs in SCA7 mice fire with a higher regularity in lobules VI and IX/X and a lower frequency in lobule VI, compared to WT littermates. Properties of PC pacemaking activity are shaped by a complex interplay between Ca2+, Na+ and K+ conductance [77] and mutations or deletions of genes encoding for these ion channels are causal factors of many types of ataxia [54]. In SCA7 mice, expression of several PC genes associated with potassium channels is downregulated (Table 1) and may explain the alterations of PC pacemaking activity [78]. This hypothesis is reinforced by the fact that in SCA7 mice PCs exhibit a higher regularity of their firing pattern (low CV2), a phenotype already observed in ataxic *waddles* mice [79]. Interestingly, in *waddles* mice, mutation in *Car8* gene leads to low CV2 of PC firing and marked ataxia syndrome in the absence of major morphological alteration of MCL, as in SCA7 mouse cerebellum. *Car8* gene is one of the 83 PC genes downregulated in SCA7 mice. Interestingly, in *waddles* mice, the low CV2 of PC activity has been restored to regular values by chlorzoxazone, a pharmacological agent increasing the probability of opening of Ca2+-dependent K+ channels [79].

The impairment of PC excitability in SCA7140Q/5Q mice is different in lobule VI and in lobule IX/X, since slowing-down of the firing frequency is only observed in lobule VI. We also observed different morphological alteration of PCs in lobule VI (smaller soma) and in lobule IX/X (altered circularity) that may be linked to their excitability impairment. In WT mice, intrinsic excitability is heterogeneous among PCs [80] and our recordings did show differences in the firing frequency between PCs located in lobule VI and in lobules IX/X. Based on the topographical organization of the olivo-cortico-cerebellar network [81], lobule-specific differences in PC firing rate between WT and SCA7 may suggest that defects are associated to specific cerebellar tasks.

Synaptic functions integrating afferent signals that arrive from CF, parallel fibers (PF) or interneurons are essential to control the output of PCs, and mutations affecting the function of synaptic circuits lead to ataxia [54]. SCA7140Q/5Q dysfunction at CF-PC synapses is revealed by the reduced vGLUT2 immunolabeling in the MCL, whereas downregulation of PC genes encoding post-synaptic membrane-associated proteins involved in glutamate signaling and LTD, such as GLURδ2 (coded by *Grid2*), GRID2ip, GABBR1 and TRPC3, indicates functional alteration of PF-PC synapses [82-85].

There is strong interest in identifying converging pathways of PC pathology across SCAs to improve our understanding of polyQ pathogenesis and to identify common potential targets for therapeutic intervention [86]. We identified 67 PC identity genes downregulated in SCA7 as well as in early symptomatic SCA1 and SCA2 mice [61, 62] (Table 1), suggesting that they are primary targets of the pathogenesis in the three SCAs. Downregulation of these PC genes points out toward alteration of LTD, cGMP-PKG signaling and phosphatidylinositol signaling pathways, with the involvement of two hub proteins, PLCB3 and PRKGI. Interestingly, PRKG1 phosphorylates PLCB3 as well as IP3R, another downregulated PC genes [87]. Deletion of *Prkg1* in PC leads to a severe decrease of LTD in PC synapses [63] and mutant mice exhibit an impaired adaptation of the vestibulo-ocular reflex, a function altered in several SCAs [88]. It is noteworthy that *Plcb3* expression is restricted to the Zebrin II positive parasagittal

stripes of the cerebellar cortex [85], suggesting that PCs located in Zebrin II positive (ZII+) stripes are particularly vulnerable in SCA1, SCA2 and SCA7. The dysfunction of ZII+ PC subclass in our SCA7140Q/5Q mice is further supported by the decreased expression of the Zebrin II gene itself (or Aldolase C, *Aldoc*) and by firing impairment of PCs located in lobule VI and IX/X of the vermis, which are enriched in ZII+ PCs.

Loss of PC identity gene expression.

Previous whole cerebellum gene profiling in polyQ SCAs models were limited to provide single-cell resolution of gene deregulation, which is constraining given the cellular heterogeneity of the cerebellum and the low percentage of PC population. Our study determined cerebellar cell-type specific gene deregulation in SCA7 mouse cerebellum. PCs differ from other cerebellar cell types by the high frequency of deregulated cell identity genes and their consistent downregulation. Many of these downregulated genes are essential for major functions of PCs – spontaneous firing and synaptic functions involving glutamate signaling and LTD – and are mutated in other genetic ataxias (Table 1).

In contrast with our understanding the gene regulatory programs that specify different neuron types during development, the programs that maintain cell-type identities in adults only begin to be delineated [89]. One emerging concept is that selective transcription factors that initially specify the acquisition of neuron-type identity continue to function later to maintain identity of postmitotic neuronal type [90]. Dysfunction of such key transcription factors is proposed to account for neurodegenerative disorders, such as Parkinson's disease [91]. In the cerebellum, RORa is highly expressed in fetal PC, is essential for their maturation [92] and is required to maintain adult PC characteristics [93]. In our study, we show that RORa expression is decreased in the cerebellum of SCA1, SCA2 and SCA7, and that many downregulated PC identity genes are indeed target of RORa, suggesting that the transcriptional program of PC maintenance involving RORa is disrupted in these polyQ SCAs. Consistently, previous studies showed that mATXN7 alters the transactivation activity of RORa in cultured cells [94], and that ATXN1 and TIP60 form a complex to control RORa activity [95]. Furthermore, postnatal loss of *Rora* expression worsened neurodegeneration of PCs in SCA1 mice [95], while increasing RORa level (through partial loss of TIP60) delayed cerebellar pathology [96].

Other mechanisms might also be involved in the loss of PC identity gene expression. Recent studies established that epigenetic regulation at super-enhancers is involved in the expression of cell identity genes [97, 98]. In Huntington's disease, it was found that neuronal identity genes regulated by super-enhancers are preferentially downregulated in the disease striatum [99]. Our study revealed that mATXN7 alters the level of both epigenetic marks (H3K9ac and H2Bub) dependent of SAGA function in SCA7 mouse cerebellum. It was previously shown that components of SAGA can be sequestered in mATXN7 aggregates [100]. mATXN7 aggregates also sequestered CBP [31], which is responsible for H3K27 acetylation, a mark of active enhancers. Therefore, further genome-wide investigation of SAGA- and CBP-dependent epigenetic marks might provide insight into mechanisms leading to loss neuron identity gene expression in SCA7.

List Of Abbreviations

Spinocerebellar ataxia type 7 (SCA7); Purkinje cells (PC); polyglutamine (polyQ); mutant ATXN7 (mATXN7); Spt-Ada-Gcn5 Acetyltransferase (SAGA); long-term depression (LTD); optical coherence tomography (OCT); electroretinography activity (ERG); outer nuclear layer (ONL); inner nuclear layer (INL); inner plexiform layer (IPL); green cone opsin (OPN1MW); blue cone opsin (OPN1SW); rhodopsin (RHO); Quantitative RT-PCR (RT-qPCR); retinal pigmented epithelium (RPE); magnetic resonance imaging (MRI); false discovery rate (FDR); wild type (WT); heterozygous (HTZ); homozygous (HMZ); males (M); females (F); Purkinje cell layer (PCL); granular cell layer (GCL); molecular cell layer (MCL); inter-spike interval (ISI); coefficient of variation for adjacent ISIs (CV2); acetylated lysine 9 of histone H3 (H3K9ac); monoubiquitinated histone H2B (H2Bub); Climbing fibers (CF); 4',6-diamidino-2-phenylindole dihydrochloride (DAPI); Paraformaldehyde (PFA); Weighted Gene Coexpression Network Analysis (WGCNA); diacylglycerol (DAG); inositol 1,4,5-triphosphate (IP3); phosphatidylinositol 4,5- bisphosphate (PIP2); a-amino-3-hydroxy-5-methyl-4-isoxazolepropionic acid receptors (AMPARs); deubiquitination module (DUB); histone acetyltransferase (HAT).

Declarations

Ethics approval and consent to participate.

All animal procedures were carried out in strict accordance with the French and German national laws for laboratory animal welfare and the guidelines of the Federation of European Laboratory Animal Science Associations, based on European Union Legislation (Directive 2010/63/EU). Experiments were approved by local Ethics Committees under the supervision of the Ministry of Higher Education, Research and Innovation in France (agreement numbers: #14199-2018032117483097, #1803-2015072215481972 and #4354-2016030212155187-v3; CREMEAS; CEEA35) and the Regierungspraesidium Tuebingen in Germany.

Consent for publication.

Not applicable.

Availability of data and materials

The RNA-seq data have been submitted to the NCBI Gene Expression Omnibus (GEO) (http://www.ncbi.nlm.nih.gov/geo/) under GSE138527 (*Link https://www.ncbi.nlm.nih.gov/geo/query/acc.cgi?acc=GSE138527 Token for reviewers: slknackkxdwfjaj*). Other datasets used and/or analyzed during the current study are available from the corresponding author on reasonable request.

Conflict of interest statement.

The authors declare no conflict of interest.

Funding.

This Project has received funding from the European Union Joint Programme–Neurodegenerative Disease Research (JPND) Project *ModelPolyQ* (Grant Agreement No. 643417) jointly funded by national funding organisations: ANR-15-JPWG-0008-03 to Y.T. and BMBF 01ED1606 to H.H.P.N.; from the E-Rare Research Programme which is a transnational R&D programme jointly funded by national funding organisations within the framework of the ERA-NET E-Rare 3 to Y.T, H.H.P.N and E.B.; from the French foundation Connaître les Syndromes Cérébelleux (CSC) to Y.T.; from ANR ANR-17-RAR3- 0008-04_ACT to Y.T.; from ANR-CE37-2015 (CeMod) and Fondation pour la Recherche Médicale (Equipes FRM DEQ20140329514) to P.I.; from ANR-10-LABX-0030-INRT under the frame programme Investissements d'Avenir labelled ANR-10-IDEX-0002-02 (to IGBMC). The 11.7T MRI scanner was funded by a grant from NeurATRIS: A Translational Research Infrastructure for Biotherapies in Neurosciences ("Investissements d'Avenir", ANR-11-INBS-0011).

Author's contributions.

ANC, EB, JF, PI, HHHN and YT conceived the project. Researchers that performed experiments and/or analyzed data: mouse behaviors (ANC, HM, AN, CW, AK, HHHN and AE), retina analyses (MJR), electromyography (FP), morphometry (ANC and BY), electrophysiology of Purkinje cells (FD and PI), MRI (JBP, JF and EB), tissue analysis and imaging (ANC, NM, MFC, AH and EG), molecular analysis (ANC, CK and AH). ANC and YT supervised the project and wrote the first draft of the manuscript. All authors read, edited and approved the manuscript.

Acknowledgments.

We thank Dr Huda Zoghbi for providing the SCA7 knock-in mice, the Mouse Clinical Institute of Illkirch for mouse phenotyping support, the GenomEast Platform at IGBMC, a member of the 'France Genomique' consortium (ANR-10-INBS-0009) for processing Illumina libraries, Stephan Collins for macro allowing PC morphological analysis, Filiz Kavla, Raphaël Bour and Christel Wagner for technical assistance, Tao Ye for fruitful discussion regarding motif enrichments, Doulaye Dembele for suggestions regarding statistical analysis. Special thanks to Nathalie Daigle and Hélène Puccio for critical reading of the manuscript and for fruitful discussion.

References

1. David G, Abbas N, Stevanin G, Durr A, Yvert G, Cancel G, et al. Cloning of the SCA7 gene reveals a highly unstable CAG repeat expansion. Nat Genet. 1997;17(1):65-70. doi: 10.1038/ng0997-
2. PubMed PMID: 9288099.
3. Niewiadomska-Cimicka A, Trottier Y. Molecular Targets and Therapeutic Strategies in Spinocerebellar Ataxia Type 7. Neurotherapeutics. 2019;16(4):1074-96. doi: 10.1007/s13311-019- 00778-5.
4. Benton CS, de Silva R, Rutledge SL, Bohlega S, Ashizawa T, Zoghbi Molecular and clinical studies in SCA-7 define a broad clinical spectrum and the infantile phenotype. Neurology. 1998;51(4):1081-6. PubMed PMID: 9781533.
5. Whitney A, Lim M, Kanabar D, Lin Massive SCA7 expansion detected in a 7-month-old male with hypotonia, cardiomegaly, and renal compromise. Dev Med Child Neurol. 2007;49(2):140-3. doi: DMCN140 [pii] 10.1111/j.1469-8749.2007.00140.x.
6. Ansorge O, Giunti P, Michalik A, Van Broeckhoven C, Harding B, Wood N, et al. Ataxin-7 aggregation and ubiquitination in infantile SCA7 with 180 CAG Ann Neurol. 2004;56(3):448-52. PubMed PMID: 15349877.
7. Trang H, Stanley SY, Thorner P, Faghfoury H, Schulze A, Hawkins C, et al. Massive CAG Repeat Expansion and Somatic Instability in Maternally Transmitted Infantile Spinocerebellar Ataxia Type 7. JAMA neurology. 2014. doi: 1001/jamaneurol.2014.1902.
8. van de Warrenburg BP, Frenken CW, Ausems MG, Kleefstra T, Sinke RJ, Knoers NV, et al. Striking anticipation in spinocerebellar ataxia type 7: the infantile phenotype. J Neurol. 2001;248(10):911-4. PubMed PMID: 11697534.
9. Helmlinger D, Hardy S, Sasorith S, Klein F, Robert F, Weber C, et al. Ataxin-7 is a subunit of GCN5 histone acetyltransferase-containing Hum Mol Genet. 2004;13(12):1257-65. PubMed PMID: 15115762.
10. David G, Durr A, Stevanin G, Cancel G, Abbas N, Benomar A, et al. Molecular and clinical correlations in autosomal dominant cerebellar ataxia with progressive macular dystrophy (SCA7). Hum Mol Genet. 1998;7(2):165-70. doi: DOI 1093/hmg/7.2.165.
11. Martin JJ. Spinocerebellar ataxia type 7. Handb Clin Neurol. 2012;103:475-91. doi: 10.1016/B978-0-444-51892-7.00030-9.
12. Rub U, Brunt ER, Seidel K, Gierga K, Mooy CM, Kettner M, et al. Spinocerebellar ataxia type 7 (SCA7): widespread brain damage in an adult-onset patient with progressive visual impairments in comparison with an adult-onset patient without visual impairments. Neuropathol Appl Neurobiol. 2008;34(2):155-68. doi: 1111/j.1365-2990.2007.00882.x.
13. Horton LC, Frosch MP, Vangel MG, Weigel-DiFranco C, Berson EL, Schmahmann Spinocerebellar ataxia type 7: clinical course, phenotype-genotype correlations, and neuropathology. Cerebellum. 2013;12(2):176-93. doi: 10.1007/s12311-012-0412-4.
14. Martin JJ, Van Regemorter N, Krols L, Brucher JM, de Barsy T, Szliwowski H, et al. On an autosomal dominant form of retinal-cerebellar degeneration: an autopsy study of five patients in one family. Acta Neuropathol (Berl). 1994;88(4):277-86. PubMed PMID:

15. Martin J, Van Regemorter N, Del-Favero J, Lofgren A, Van Broeckhoven C. Spinocerebellar ataxia type 7 (SCA7) - correlations between phenotype and genotype in one large Belgian family. J Neurol Sci. 1999;168(1):37-46. PubMed PMID:
16. Alcauter S, Barrios FA, Diaz R, Fernandez-Ruiz J. Gray and white matter alterations in spinocerebellar ataxia type 7: an in vivo DTI and VBM study. Neuroimage. 2011;55(1):1-7. doi: 10.1016/j.neuroimage.2010.12.014.
17. Bang OY, Lee PH, Kim SY, Kim HJ, Huh Pontine atrophy precedes cerebellar degeneration in spinocerebellar ataxia 7: MRI-based volumetric analysis. J Neurol Neurosurg Psychiatry. 2004;75(10):1452-6. PubMed PMID: 15377695.
18. Michalik A, Martin JJ, Van Broeckhoven C. Spinocerebellar ataxia type 7 associated with pigmentary retinal dystrophy. Eur J Hum Genet. 2004;12(1):2-15. PubMed PMID:

18. Salas-Vargas J, Mancera-Gervacio J, Velazquez-Perez L, Rodrigez-Labrada R, Martinez-Cruz E, Magana JJ, et al. Spinocerebellar ataxia type 7: a neurodegenerative disorder with peripheral neuropathy. Eur Neurol. 2015;73(3-4):173-8. doi: 1159/000370239.
19. van de Warrenburg BP, Notermans NC, Schelhaas HJ, van Alfen N, Sinke RJ, Knoers NV, et al. Peripheral nerve involvement in spinocerebellar ataxias. Arch Neurol. 2004;61(2):257-61. doi: 10.1001/archneur.61.2.257.
20. Aleman TS, Cideciyan AV, Volpe NJ, Stevanin G, Brice A, Jacobson Spinocerebellar ataxia type 7 (SCA7) shows a cone-rod dystrophy phenotype. Exp Eye Res. 2002;74(6):737-45. PubMed PMID: 12126946.
21. La Spada AR, Fu YH, Sopher BL, Libby RT, Wang X, Li LY, et al. Polyglutamine-expanded ataxin-7 antagonizes CRX function and induces cone-rod dystrophy in a mouse model of Neuron. 2001;31(6):913-27. PubMed PMID: 11580893.
22. Abou-Sleymane G, Chalmel F, Helmlinger D, Lardenois A, Thibault C, Weber C, et Polyglutamine expansion causes neurodegeneration by altering the neuronal differentiation program. Hum Mol Genet. 2006;15(5):691-703. PubMed PMID: 16434483.
23. Helmlinger D, Hardy S, Abou-Sleymane G, Eberlin A, Bowman AB, Gansmuller A, et al. Glutamine-expanded ataxin-7 alters TFTC/STAGA recruitment and chromatin structure leading to photoreceptor dysfunction. PLoS Biol. 2006;4(3):e67. PubMed PMID:
24. Yefimova MG, Messaddeq N, Karam A, Jacquard C, Weber C, Jonet L, et Polyglutamine toxicity induces rod photoreceptor division, morphological transformation or death in Spinocerebellar ataxia 7 mouse retina. Neurobiol Dis. 2010;40(1):311-24. doi: S0969-9961(10)00201-9 [pii] 10.1016/j.nbd.2010.06.005.
25. Palhan VB, Chen S, Peng GH, Tjernberg A, Gamper AM, Fan Y, et Polyglutamine-expanded ataxin-7 inhibits STAGA histone acetyltransferase activity to produce retinal degeneration. Proc Natl Acad Sci U S A. 2005;102(24):8472-7. PubMed PMID: 15932940.

26. Chen S, Peng GH, Wang X, Smith AC, Grote SK, Sopher BL, et al. Interference of Crx- dependent transcription by ataxin-7 involves interaction between the glutamine regions and requires the ataxin-7 carboxy-terminal region for nuclear localization. Hum Mol Genet. 2004;13(1):53-67. PubMed PMID:
27. Merienne K, Friedman J, Akimoto M, Abou-Sleymane G, Weber C, Swaroop A, et Preventing polyglutamine-induced activation of c-Jun delays neuronal dysfunction in a mouse model of SCA7 retinopathy. Neurobiol Dis. 2007;25(3):571-81. Epub 2006/12/27. doi: S0969-9961(06)00292-0 [pii] 10.1016/j.nbd.2006.11.002.
28. Carrillo-Rosas S, Weber C, Fievet L, Messaddeq N, Karam A, Trottier Y. Loss of zebrafish Ataxin-7, a SAGA subunit responsible for SCA7 retinopathy, causes ocular coloboma and malformation of photoreceptors. Hum Mol Genet. 2018. doi: 10.1093/hmg/ddy401 1093/hmg/ddy401.
29. Yanicostas C, Barbieri E, Hibi M, Brice A, Stevanin G, Soussi-Yanicostas N. Requirement for zebrafish ataxin-7 in differentiation of photoreceptors and cerebellar neurons. PLoS One. 2012;7(11):e50705. doi: 10.1371/journal.pone.0050705 PONE-D-12-11658 [pii].
30. Yvert G, Lindenberg KS, Picaud S, Landwehrmeyer GB, Sahel JA, Mandel JL. Expanded polyglutamines induce neurodegeneration and trans-neuronal alterations in cerebellum and retina of SCA7 transgenic mice. Hum Mol Genet. 2000;9(17):2491-506. PubMed PMID:
31. Yvert G, Lindenberg KS, Devys D, Helmlinger D, Landwehrmeyer GB, Mandel SCA7 mouse models show selective stabilization of mutant ataxin-7 and similar cellular responses in different neuronal cell types. Hum Mol Genet. 2001;10(16):1679-92. PubMed PMID: 11487572.
32. Chou AH, Chen CY, Chen SY, Chen WJ, Chen YL, Weng YS, et al. Polyglutamine-expanded ataxin-7 causes cerebellar dysfunction by inducing transcriptional dysregulation. Neurochemistry international. 2010;56(2):329-39. doi: 1016/j.neuint.2009.11.003.
33. Custer SK, Garden GA, Gill N, Rueb U, Libby RT, Schultz C, et Bergmann glia expression of polyglutamine-expanded ataxin-7 produces neurodegeneration by impairing glutamate transport. Nat Neurosci. 2006;9(10):1302-11. PubMed PMID: 16936724.
34. Mookerjee S, Papanikolaou T, Guyenet SJ, Sampath V, Lin A, Vitelli C, et al. Posttranslational modification of ataxin-7 at lysine 257 prevents autophagy-mediated turnover of an N-terminal caspase- 7 cleavage fragment. J Neurosci. 2009;29(48):15134-44. Epub 2009/12/04. doi: 29/48/15134 [pii] 10.1523/JNEUROSCI.4720-09.2009.
35. Furrer SA, Waldherr SM, Mohanachandran MS, Baughn TD, Nguyen KT, Sopher BL, et Reduction of mutant ataxin-7 expression restores motor function and prevents cerebellar synaptic reorganization in a conditional mouse model of SCA7. Hum Mol Genet. 2013;22(5):890-903. doi: 10.1093/hmg/dds495.
36. Karam A, Trottier Y. Molecular Mechanisms and Therapeutic Strategies in Spinocerebellar Ataxia Type Adv Exp Med Biol. 2018;1049:197-218. doi: 10.1007/978-3-319-71779-1_9 10.1007/978-3-319-71779-1_9. PubMed PMID: 29427104.
37. Friedrich B, Euler P, Ziegler R, Kuhn A, Landwehrmeyer BG, Luthi-Carter R, et Comparative analyses of Purkinje cell gene expression profiles reveal shared molecular abnormalities in models of different

polyglutamine diseases. Brain Res. 2012;1481:37-48. doi: 10.1016/j.brainres.2012.08.005.

38. Stoyas CA, Bushart DD, Switonski PM, Ward JM, Alaghatta A, Tang MB, et al. Nicotinamide Pathway-Dependent Sirt1 Activation Restores Calcium Homeostasis to Achieve Neuroprotection in Spinocerebellar Ataxia Type Neuron. 2020;105(4):630-44 e9. doi: 10.1016/j.neuron.2019.11.019.
39. Yoo SY, Pennesi ME, Weeber EJ, Xu B, Atkinson R, Chen S, et al. SCA7 knockin mice model human SCA7 and reveal gradual accumulation of mutant ataxin-7 in neurons and abnormalities in short-term plasticity. Neuron. 2003;37(3):383-401. PubMed PMID:
40. Chen YC, Gatchel JR, Lewis RW, Mao CA, Grant PA, Zoghbi HY, et al. Gcn5 loss-of-function accelerates cerebellar and retinal degeneration in a SCA7 mouse model. Hum Mol Genet. 2012;21(2):394-405. Epub 2011/10/18. doi: ddr474 [pii] 1093/hmg/ddr474.
41. Klockgether T. Update on degenerative ataxias. Curr Opin Neurol. 2011;24(4):339-45. Epub 2011/07/08. doi: 1097/WCO.0b013e32834875ba.
42. Niewiadomska-Cimicka A, Hache A, Trottier Gene Deregulation and Underlying Mechanisms in Spinocerebellar Ataxias With Polyglutamine Expansion. Front Neurosci. 2020;14:571. doi: 10.3389/fnins.2020.00571.
43. Mikhaleva A, Kannan M, Wagner C, Yalcin Histomorphological Phenotyping of the Adult Mouse Brain. Curr Protoc Mouse Biol. 2016;6(3):307-32. doi: 10.1002/cpmo.12. PubMed PMID: 27584555.
44. Dhenain M, Delatour B, Walczak C, Volk Passive staining: a novel ex vivo MRI protocol to detect amyloid deposits in mouse models of Alzheimer's disease. Magn Reson Med. 2006;55(3):687- 93. doi: 10.1002/mrm.20810.
45. Lein ES, Hawrylycz MJ, Ao N, Ayres M, Bensinger A, Bernard A, et al. Genome-wide atlas of gene expression in the adult mouse brain. Nature. 2007;445(7124):168-76. doi: 10.1038/nature05453 10.1038/nature05453.
46. Kim D, Pertea G, Trapnell C, Pimentel H, Kelley R, Salzberg SL. TopHat2: accurate alignment of transcriptomes in the presence of insertions, deletions and gene fusions. Genome Biol. 2013;14(4):R36. doi: 1186/gb-2013-14-4-r36.
47. Anders S, Pyl PT, Huber W. HTSeq–a Python framework to work with high-throughput sequencing data. Bioinformatics. 2015;31(2):166-9. doi: 1093/bioinformatics/btu638.
48. Love MI, Huber W, Anders Moderated estimation of fold change and dispersion for RNA-seq data with DESeq2. Genome Biol. 2014;15(12):550. doi: 10.1186/s13059-014-0550-8.
49. Szklarczyk D, Franceschini A, Wyder S, Forslund K, Heller D, Huerta-Cepas J, et al. STRING v10: protein-protein interaction networks, integrated over the tree of life. Nucleic Acids Res. 2015;43(Database issue):D447-52. doi: 1093/nar/gku1003.
50. Kramer A, Green J, Pollard J, Jr., Tugendreich S. Causal analysis approaches in Ingenuity Pathway Analysis. Bioinformatics. 2014;30(4):523-30. doi: 1093/bioinformatics/btt703.
51. Doyle JP, Dougherty JD, Heiman M, Schmidt EF, Stevens TR, Ma G, et al. Application of a translational profiling approach for the comparative analysis of CNS cell types. Cell. 2008;135(4):749- 62. doi: 1016/j.cell.2008.10.029.

52. Gruol DL, Franklin CL. Morphological and physiological differentiation of Purkinje neurons in cultures of rat J Neurosci. 1987;7(5):1271-93. PubMed PMID: 2437259.
53. Hausser M, Clark BA. Tonic synaptic inhibition modulates neuronal output pattern and spatiotemporal synaptic Neuron. 1997;19(3):665-78. doi: 10.1016/s0896-6273(00)80379-7.
54. Hoxha E, Balbo I, Miniaci MC, Tempia F. Purkinje Cell Signaling Deficits in Animal Models of Front Synaptic Neurosci. 2018;10:6. doi: 10.3389/fnsyn.2018.00006.
55. Arancillo M, White JJ, Lin T, Stay TL, Sillitoe In vivo analysis of Purkinje cell firing properties during postnatal mouse development. J Neurophysiol. 2015;113(2):578-91. doi: 10.1152/jn.00586.2014.
56. Holt GR, Softky WR, Koch C, Douglas RJ. Comparison of discharge variability in vitro and in vivo in cat visual cortex neurons. J Neurophysiol. 1996;75(5):1806-14. doi: 10.1152/jn.1996.75.5.1806 10.1152/jn.1996.75.5.1806.
57. Chort A, Alves S, Marinello M, Dufresnois B, Dornbierer JG, Tesson C, et al. Interferon beta induces clearance of mutant ataxin 7 and improves locomotion in SCA7 knock-in mice. Brain. 2013. Epub 2013/03/23. doi: awt061 [pii] 1093/brain/awt061.
58. Kratz A, Beguin P, Kaneko M, Chimura T, Suzuki AM, Matsunaga A, et al. Digital expression profiling of the compartmentalized translatome of Purkinje neurons. Genome Res. 2014;24(8):1396- 410. doi: 1101/gr.164095.113.
59. Sato A, Sekine Y, Saruta C, Nishibe H, Morita N, Sato Y, et al. Cerebellar development transcriptome database (CDT-DB): profiling of spatio-temporal gene expression during the postnatal development of mouse cerebellum. Neural Netw. 2008;21(8):1056-69. doi: 10.1016/j.neunet.2008.05.004.
60. Dansithong W, Paul S, Figueroa KP, Rinehart MD, Wiest S, Pflieger LT, et Ataxin-2 regulates RGS8 translation in a new BAC-SCA2 transgenic mouse model. PLoS Genet. 2015;11(4):e1005182. doi: 10.1371/journal.pgen.1005182.
61. Ingram M, Wozniak EAL, Duvick L, Yang R, Bergmann P, Carson R, et al. Cerebellar Transcriptome Profiles of ATXN1 Transgenic Mice Reveal SCA1 Disease Progression and Protection Pathways. Neuron. 2016;89(6):1194-207. doi: 1016/j.neuron.2016.02.011.
62. Hansen ST, Meera P, Otis TS, Pulst SM. Changes in Purkinje cell firing and gene expression precede behavioral pathology in a mouse model of Human molecular genetics. 2013;22(2):271- 83. doi: 10.1093/hmg/dds427.
63. Feil R, Hartmann J, Luo C, Wolfsgruber W, Schilling K, Feil S, et Impairment of LTD and cerebellar learning by Purkinje cell-specific ablation of cGMP-dependent protein kinase I. J Cell Biol. 2003;163(2):295-302. doi: 10.1083/jcb.200306148.
64. Gold DA, Baek SH, Schork NJ, Rose DW, Larsen DD, Sachs BD, et al. RORalpha coordinates reciprocal signaling in cerebellar development through sonic hedgehog and calcium-dependent pathways. Neuron. 2003;40(6):1119-31. doi: 1016/s0896-6273(03)00769-4.
65. Sarachana T, Hu VW. Genome-wide identification of transcriptional targets of RORA reveals direct regulation of multiple genes associated with autism spectrum Mol Autism. 2013;4(1):14. doi:

10.1186/2040-2392-4-14.

66. Bailey TL, Boden M, Buske FA, Frith M, Grant CE, Clementi L, et al. MEME SUITE: tools for motif discovery and searching. Nucleic Acids 2009;37(Web Server issue):W202-8. doi: 10.1093/nar/gkp335.
67. Swaroop A, Kim D, Forrest Transcriptional regulation of photoreceptor development and homeostasis in the mammalian retina. Nat Rev Neurosci. 2010;11(8):563-76. doi: 10.1038/nrn2880.
68. Marmorstein LY, McLaughlin PJ, Peachey NS, Sasaki T, Marmorstein AD. Formation and progression of sub-retinal pigment epithelium deposits in Efemp1 mutation knock-in mice: a model for the early pathogenic course of macular degeneration. Hum Mol Genet. 2007;16(20):2423-32. doi: 10.1093/hmg/ddm199.
69. Kahle JJ, Gulbahce N, Shaw CA, Lim J, Hill DE, Barabasi AL, et Comparison of an expanded ataxia interactome with patient medical records reveals a relationship between macular degeneration and ataxia. Human molecular genetics. 2011;20(3):510-27. doi: 10.1093/hmg/ddq496.
70. Adanyeguh IM, Perlbarg V, Henry PG, Rinaldi D, Petit E, Valabregue R, et al. Autosomal dominant cerebellar ataxias: Imaging biomarkers with high effect Neuroimage Clin. 2018;19:858- 67. doi: 10.1016/j.nicl.2018.06.011.
71. Hernandez-Castillo CR, Alcauter S, Galvez V, Barrios FA, Yescas P, Ochoa A, et Disruption of visual and motor connectivity in spinocerebellar ataxia type 7. Mov Disord. 2013;28(12):1708-16. doi: 10.1002/mds.25618.
72. Hernandez-Castillo CR, Galvez V, Diaz R, Fernandez-Ruiz J. Specific cerebellar and cortical degeneration correlates with ataxia severity in spinocerebellar ataxia type 7. Brain Imaging Behav. 2016;10(1):252-7. doi: 1007/s11682-015-9389-1.
73. Chirino A, Hernandez-Castillo CR, Galvez V, Contreras A, Diaz R, Beltran-Parrazal L, et Motor and cognitive impairments in spinocerebellar ataxia type 7 and its correlations with cortical volumes. The European journal of neuroscience. 2018;48(10):3199-211. doi: 10.1111/ejn.14148.
74. Dorgans K, Salvi J, Bertaso F, Bernard L, Lory P, Doussau F, et al. Characterization of the dominant inheritance mechanism of Episodic Ataxia type Neurobiol Dis. 2017;106:110-23. doi: 10.1016/j.nbd.2017.07.004.
75. Stahl JS, Thumser ZC. Flocculus Purkinje cell signals in mouse Cacna1a calcium channel mutants of escalating severity: an investigation of the role of firing irregularity in ataxia. J Neurophysiol. 2014;112(10):2647-63. doi: 1152/jn.00129.2014.
76. Stefely JA, Licitra F, Laredj L, Reidenbach AG, Kemmerer ZA, Grangeray A, et al. Cerebellar Ataxia and Coenzyme Q Deficiency through Loss of Unorthodox Kinase Activity. Mol Cell. 2016;63(4):608-20. doi: 1016/j.molcel.2016.06.030.
77. Raman IM, Bean BP. Ionic currents underlying spontaneous action potentials in isolated cerebellar Purkinje neurons. J Neurosci. 1999;19(5):1663-74. PubMed PMID:

78. Bushart DD, Shakkottai VG. Ion channel dysfunction in cerebellar ataxia. Neurosci Lett. 2019;688:41-8. doi: 1016/j.neulet.2018.02.005.
79. White JJ, Arancillo M, King A, Lin T, Miterko LN, Gebre SA, et Pathogenesis of severe ataxia and tremor without the typical signs of neurodegeneration. Neurobiol Dis. 2016;86:86-98. doi: 10.1016/j.nbd.2015.11.008.
80. Zhou H, Lin Z, Voges K, Ju C, Gao Z, Bosman LW, et Cerebellar modules operate at different frequencies. Elife. 2014;3:e02536. doi: 10.7554/eLife.02536.
81. Apps R, Hawkes Cerebellar cortical organization: a one-map hypothesis. Nat Rev Neurosci. 2009;10(9):670-81. doi: 10.1038/nrn2698.
82. Kashiwabuchi N, Ikeda K, Araki K, Hirano T, Shibuki K, Takayama C, et Impairment of motor coordination, Purkinje cell synapse formation, and cerebellar long-term depression in GluR delta 2 mutant mice. Cell. 1995;81(2):245-52. doi: 10.1016/0092-8674(95)90334-8.
83. Kato AS, Knierman MD, Siuda ER, Isaac JT, Nisenbaum ES, Bredt Glutamate receptor delta2 associates with metabotropic glutamate receptor 1 (mGluR1), protein kinase Cgamma, and canonical transient receptor potential 3 and regulates mGluR1-mediated synaptic transmission in cerebellar Purkinje neurons. J Neurosci. 2012;32(44):15296-308. doi: 10.1523/JNEUROSCI.0705-12.2012.
84. Tabata T, Araishi K, Hashimoto K, Hashimotodani Y, van der Putten H, Bettler B, et al. Ca2+ activity at GABAB receptors constitutively promotes metabotropic glutamate signaling in the absence of GABA. Proc Natl Acad Sci U S 2004;101(48):16952-7. doi: 10.1073/pnas.0405387101.
85. Hawkes R. Purkinje cell stripes and long-term depression at the parallel fiber-Purkinje cell synapse. Front Syst Neurosci. 2014;8:41. doi: 10.3389/fnsys.2014.00041.
86. Smeets CJ, Verbeek DS. Cerebellar ataxia and functional genomics: Identifying the routes to cerebellar neurodegeneration. Biochim Biophys Acta. 2014;1842(10):2030-8. doi: 10.1016/j.bbadis.2014.04.004.
87. Francis SH, Busch JL, Corbin JD, Sibley D. cGMP-dependent protein kinases and cGMP phosphodiesterases in nitric oxide and cGMP action. Pharmacol Rev. 2010;62(3):525-63. doi: 10.1124/pr.110.002907.
88. Parker JL, Santiago M. Oculomotor aspects of the hereditary cerebellar ataxias. Handb Clin Neurol. 2012;103:63-83. doi: 1016/B978-0-444-51892-7.00003-6.
89. Holmberg J, Perlmann T. Maintaining differentiated cellular identity. Nat Rev Genet. 2012;13(6):429-39. doi: 1038/nrg3209.
90. Deneris ES, Hobert O. Maintenance of postmitotic neuronal cell identity. Nat Neurosci. 2014;17(7):899-907. doi: 1038/nn.3731.
91. Decressac M, Kadkhodaei B, Mattsson B, Laguna A, Perlmann T, Bjorklund alpha-Synuclein- induced down-regulation of Nurr1 disrupts GDNF signaling in nigral dopamine neurons. Sci Transl Med. 2012;4(163):163ra56. doi: 10.1126/scitranslmed.3004676.

92. Boukhtouche F, Doulazmi M, Frederic F, Dusart I, Brugg B, Mariani J. RORalpha, a pivotal nuclear receptor for Purkinje neuron survival and differentiation: from development to ageing. Cerebellum. 2006;5(2):97-104. doi: 1080/14734220600750184.
93. Chen XR, Heck N, Lohof AM, Rochefort C, Morel MP, Wehrle R, et al. Mature Purkinje cells require the retinoic acid-related orphan receptor-alpha (RORalpha) to maintain climbing fiber mono- innervation and other adult characteristics. J Neurosci. 2013;33(22):9546-62. doi: 10.1523/JNEUROSCI.2977-12.2013.
94. Strom AL, Forsgren L, Holmberg M. A role for both wild-type and expanded ataxin-7 in transcriptional regulation. Neurobiol Dis. 2005;20(3):646-55. PubMed PMID:
95. Serra HG, Duvick L, Zu T, Carlson K, Stevens S, Jorgensen N, et al. RORalpha-mediated Purkinje cell development determines disease severity in adult SCA1 mice. Cell. 2006;127(4):697-708. doi: 1016/j.cell.2006.09.036.
96. Gehrking KM, Andresen JM, Duvick L, Lough J, Zoghbi HY, Orr HT. Partial loss of Tip60 slows mid-stage neurodegeneration in a spinocerebellar ataxia type 1 (SCA1) mouse model. Human molecular genetics. 2011;20(11):2204-12. doi: 1093/hmg/ddr108.
97. Hnisz D, Abraham BJ, Lee TI, Lau A, Saint-Andre V, Sigova AA, et al. Super-enhancers in the control of cell identity and disease. Cell. 2013;155(4):934-47. doi: 1016/j.cell.2013.09.053.
98. Whyte WA, Orlando DA, Hnisz D, Abraham BJ, Lin CY, Kagey MH, et al. Master transcription factors and mediator establish super-enhancers at key cell identity genes. Cell. 2013;153(2):307-19. doi: 1016/j.cell.2013.03.035.
99. Achour M, Le Gras S, Keime C, Parmentier F, Lejeune FX, Boutillier AL, et Neuronal identity genes regulated by super-enhancers are preferentially down-regulated in the striatum of Huntington's disease mice. Hum Mol Genet. 2015;24(12):3481-96. doi: 10.1093/hmg/ddv099.
100. Lan X, Koutelou E, Schibler AC, Chen YC, Grant PA, Dent SY. Poly(Q) Expansions in ATXN7 Affect Solubility but Not Activity of the SAGA Deubiquitinating Module. Molecular and cellular biology. 2015;35(10):1777-87. doi: 1128/MCB.01454-14.

Table

Please see the supplementary files section to view the table.

Figures

Figure 1

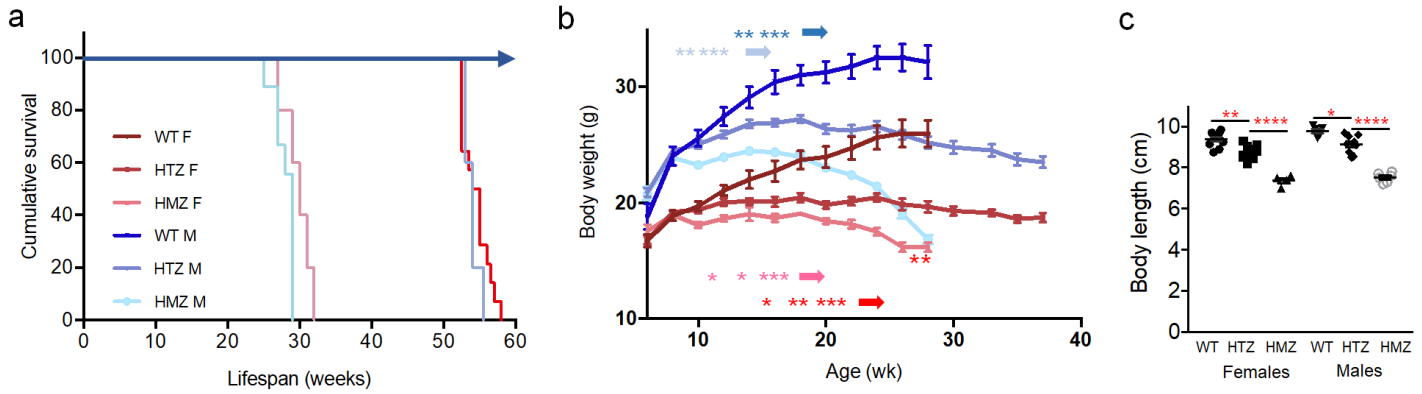

Figure 1

Lifespan and body size of SCA7 mice. a Kaplan-Meier survival curves indicate that SCA7140Q/5Q heterozygous (HTZ) and SCA7140Q/140Q homozygous (HMZ) males (M) and females (F) have shorter lifespan than wild type (WT) littermates; n= WT F: 11; WT M: 5; HTZ F: 9; HTZ M: 4; HMZ F: 6; HMZ M: 5. b Gain in body weight of females and males of SCA7 HTZ and SCA7 HMZ mice differs from WT littermates; n= WT F: 11; WT M: 5; HTZ F: 8; HTZ M:9; HMZ F:6; HMZ M:9). c Body length of 38-week old females and males of WT, SCA7 HTZ and SCA7 HMZ mice. Data are expressed as mean ± SEM. b, Two-way ANOVA with repeated measurement followed by post-hoc Bonferroni test. c, One-way ANOVA followed by post-hoc Bonferroni test. *p<0.05; **p<0.01; ***p<0.001; ****p<0.0001.

Figure 2

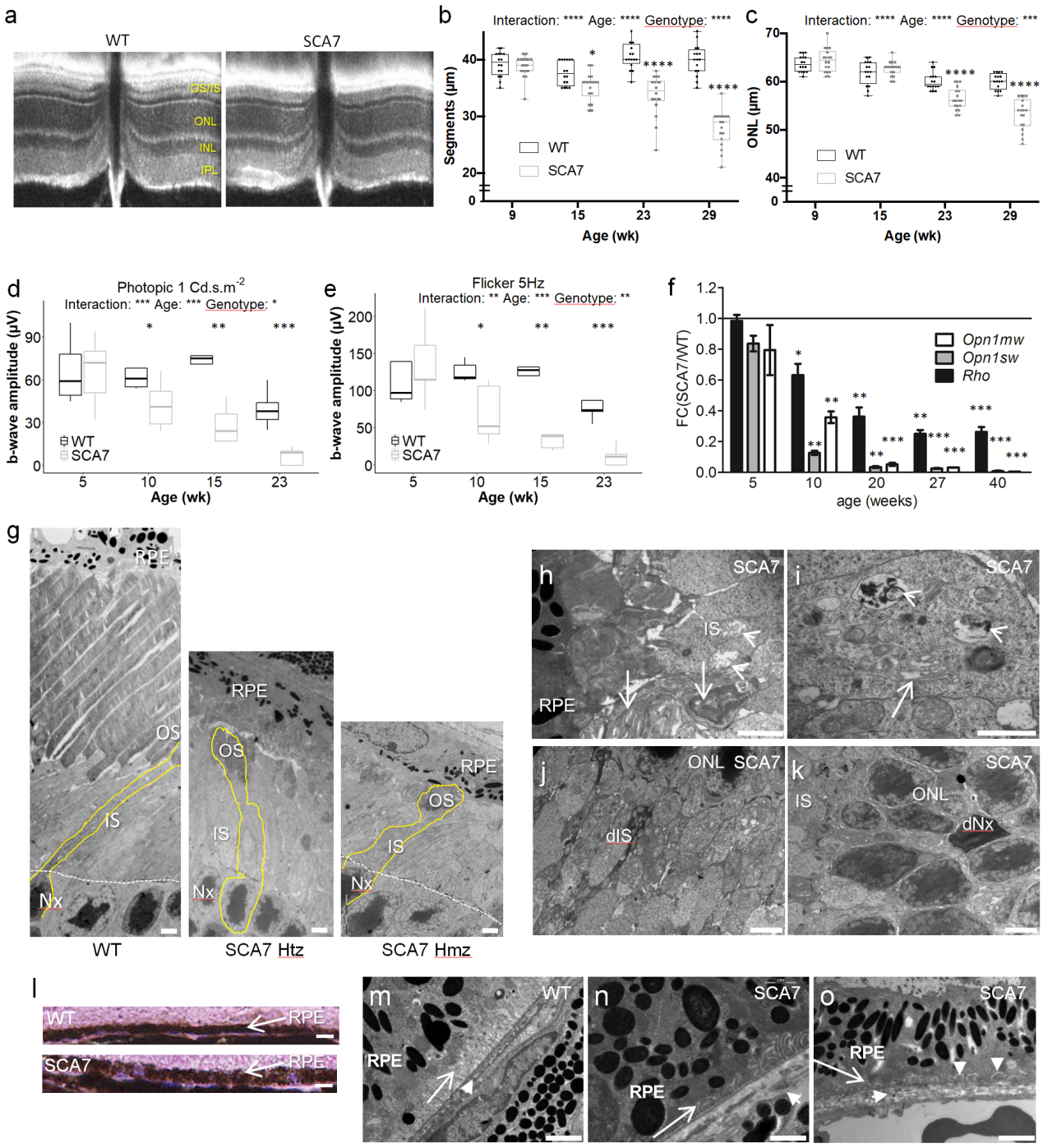

Figure 2

Photoreceptor and retinal pigmented epithelium degeneration in SCA7 mice. a Representative optical coherence tomography (OCT) B-scan showing reduced thickness of the segment layers of SCA7140Q/5Q mice compared to wild type (WT) at 29 weeks (wk). Outer segment (OS) and inner segment (IS), outer nuclear layer (ONL) inner nuclear layer (INL), inner plexiform layer (IPL). b-c Longitudinal OCT measurements show progressive thinning of photoreceptor segment layers (b) and ONL (c) in

SCA7140Q/5Q mice relative to WT littermates; n= both eyes of 8 WT and 9 SCA7 mice. d-e Longitudinal cone-derived b-wave amplitudes of photopic response to 1 Cd.s.m-2 flashes (d) and 5 Hz flicker responses to 3 Cd.s.m-2 flashes (e) show progressive reduction of cone function in SCA7140Q/5Q retina relative to WT retina; n= single eyes of 5 WT and 5 SCA7 mice. Background illumination was 25 Cd.m-2. f Quantitative RT-PCR analysis shows early and progressive downregulation of Opn1mw and Opn1sw cone genes and Rhodopsin (Rho) rod gene in SCA7140Q/5Q retina, as shown by normalization to WT gene expression levels; n= 3-6/genotype. g Electron micrographs showing the progressive disappearance of OS and the shortening of IS of 44 wk-old SCA7 heterozygotes (Htz) and 20 wk-old SCA7 homozygotes (Hmz), compared to WT mice. Retinal pigmented epithelium (RPE), photoreceptor nuclei (Nx). Scale bar = 10 µm. h-k Electron micrographs of 20 wk-old SCA7140Q/140Q retina. h, the remnant OS have lost their parallel organization (arrows) and the IS contain swollen and disrupted mitochondria (arrowheads). i, The IS shows dilated and vesiculated endoplasmic reticulum (arrow) and accumulation of vesicular membranes (arrowhead). j, Dark degenerating IS (dIS) with numerous abnormal mitochondria. k, Dark photoreceptor nuclei (dNx). Scale bar: 2 µm (H, I) and 5 µm (J, K). l Histological sections comparing the thickness of WT and SCA7 RPE at 20 wk. Scale bar = 15 µm. m-o, Electron micrographs comparing the basal infolding membrane of RPE and Bruch's membrane of WT and SCA7 mice. In WT (m), the basal infolding membrane of RPE (arrow) shows a typical lamellar organization with translucid lumen, and a regular Bruch's membrane (arrowhead). In contrast in SCA7 retina, the infolding membrane (long arrow) is either opaque (n) or completely absent (o), while the Bruch's membrane (short arrow) is enlarged and disorganized (n, o), and occasionally interrupted (n). In addition, homogenous deposits are found between the basement membrane and plasma membrane of RPE (vertical arrowheads in O). Scale bar = 2 µm. Data are expressed as mean ± SEM and analyzed using Student's t-test in f; box-and-whisker plot and two-way ANOVA with repeated measurement followed by post-hoc Bonferroni test in b-e.: *$p<0.05$; **$p<0.01$; ***$p<0.001$

Figure 3

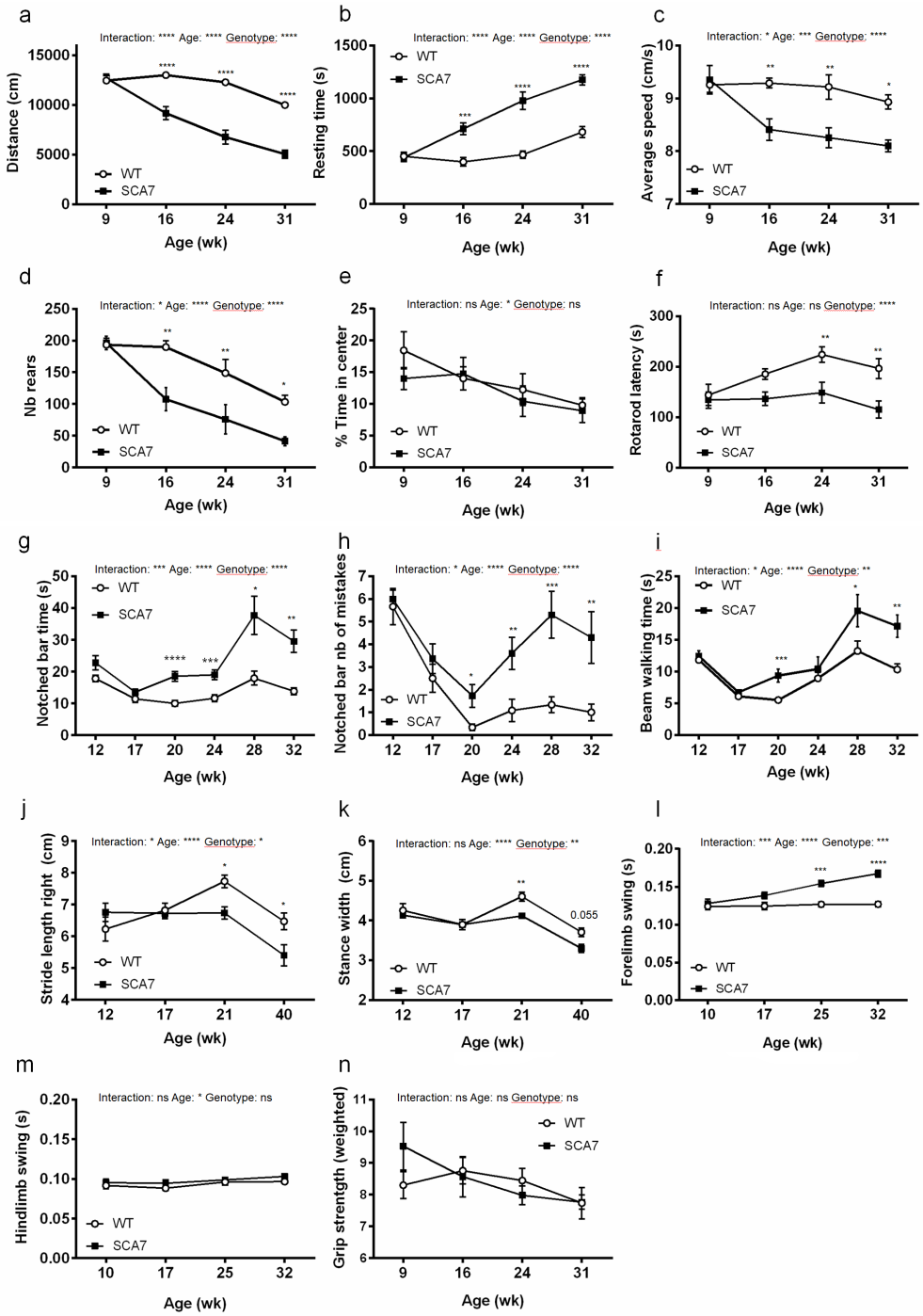

Figure 3

Behavioral and motor deficits of SCA7 mice. a-e Open field analyses show that SCA7140Q/5Q males (n= 6) progressively become hypoactive relative to wild type (WT) male littermates (n= 6), according to the distance travelled (a), the resting time (b), the average speed (c) and the number (Nb) of rears (d). However, SCA7 mice show no difference with WT mice as for the time spent in the arena center (e). Centimeter (cm), second (s), week (wk). f Accelerating rotarod (mean latency to fall) shows progressive

motor deficit of SCA7140Q/5Q mice (n= 6) compared to WT littermates (n= 6). g-h Notched bar (time to cross the bar (g) and number of mistakes (h)) indicates that SCA7140Q/5Q mice (n= 10) progressively have altered motor coordination and balance compared to WT littermates (n= 12). i Beam walking also shows that motor performances of SCA7140Q/5Q (n= 6) mice are affected compared to WT littermates (n= 6). j-k Spatial gait analysis using footprint patterns indicates that SCA7140Q/5Q mice (n= 9-11) progressively have shorter stride length of the four limbs (right forelimb illustrated in j) and shorter stance width (forelimbs illustrated in k) compared to WT littermates (n= 9-12). l-m Temporal gait analysis using Catwalk shows that swing times of forelimbs (average of right and left forelimbs in l), but not hindlimbs (average of right and left hindlimbs in m) of SCA7140Q/5Q mice (n= 15) progressively become slower than those of WT littermates (n=10). n Grip strength performance of SCA7140Q/5Q mice (n= 6) normalized by mouse body weight is similar to WT mice (n= 6). Data are expressed as mean ± SEM. Two-way ANOVA with repeated measurement (a-i, l-n) or ordinary two-way ANOVA (j, k), followed by post-hoc Bonferroni test: *$p<0.05$; **$p<0.01$; ***$p<0.001$; ****$p<0.0001$; ns= not significant.

Figure 4

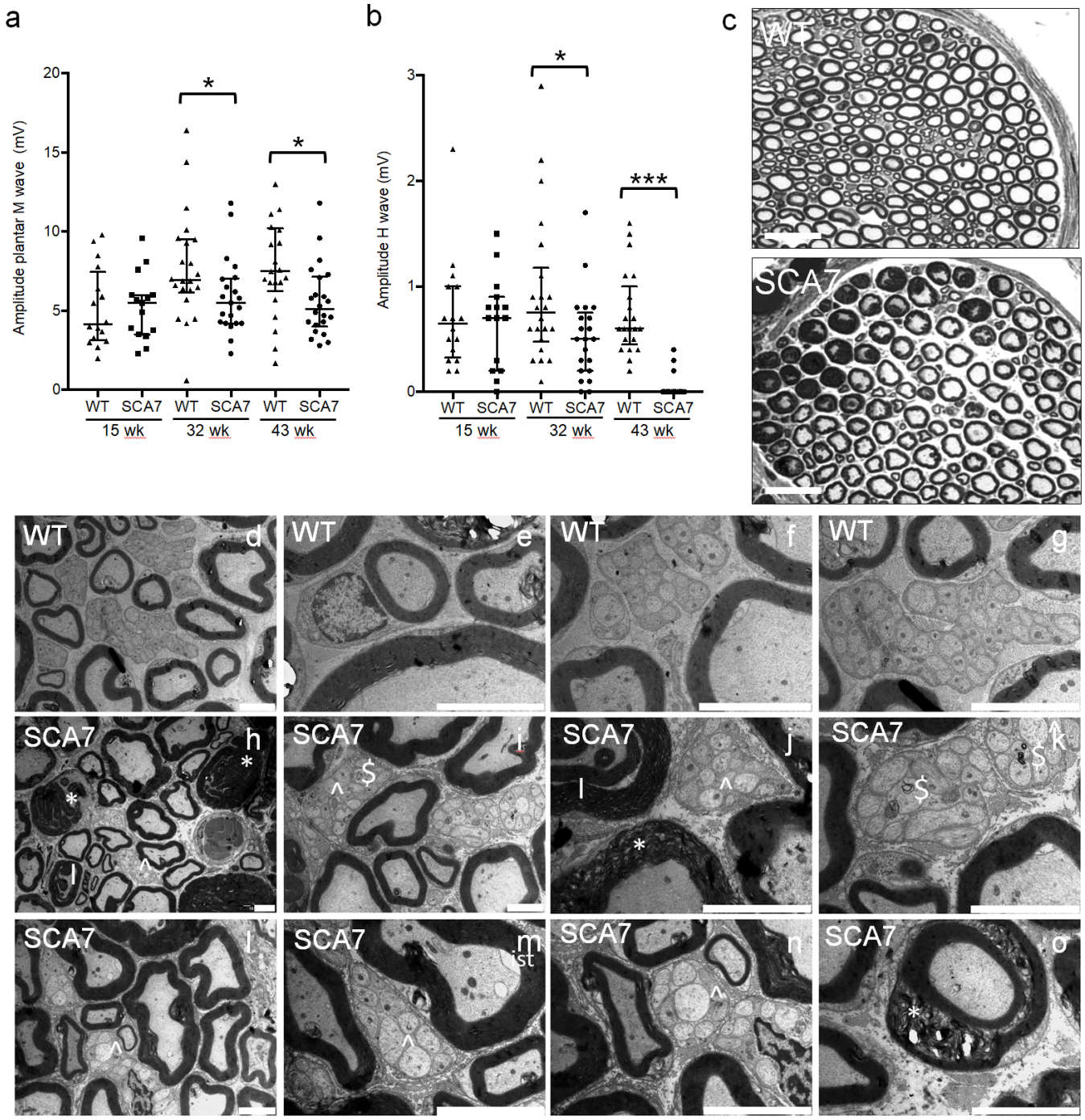

Figure 4

Peripheral nerve alterations in SCA7 mice. a, b Electromyograph activities of the sciatic nerve. Amplitude of motor M-wave (a) and sensory H-wave (b) in SCA7140Q/5Q mice relative to wild type (WT) littermates (15 weeks (wk): n= 16 WT and 15 SCA7; 32 wk: n= 22 WT and 21 SCA7; 43 wk: n= 22 WT and 21 SCA7). Scatter plot showing median with interquartile range. Mann-Whitney test: *p<0.05, ***p<0.001. c Comparison of semithin sections of sciatic nerve of SCA7140Q/5Q and WT mice. The mutant shows

irregular and degenerated myelinated fibers and loss of small fibers. Scale bars, 50µm d-o Electron microscopy analyses of the sciatic nerve. Compared to WT littermates (d-g), sciatic nerve section of SCA7140Q/5Q mice (h-o) at 43 wk shows severe abnormalities in both myelinated and non-myelinated fibers including myelin degeneration (* in h, j, o), infolding like structure (I in h, j), abnormal Remak bundle (^ in h-j, l-n), autophagy ($ in i, k), inner swelling tongue (ist in m). Scales bar: D, M and N = 5µm; E-G, I-L and O = 2µm; H = 10µm.

Figure 5

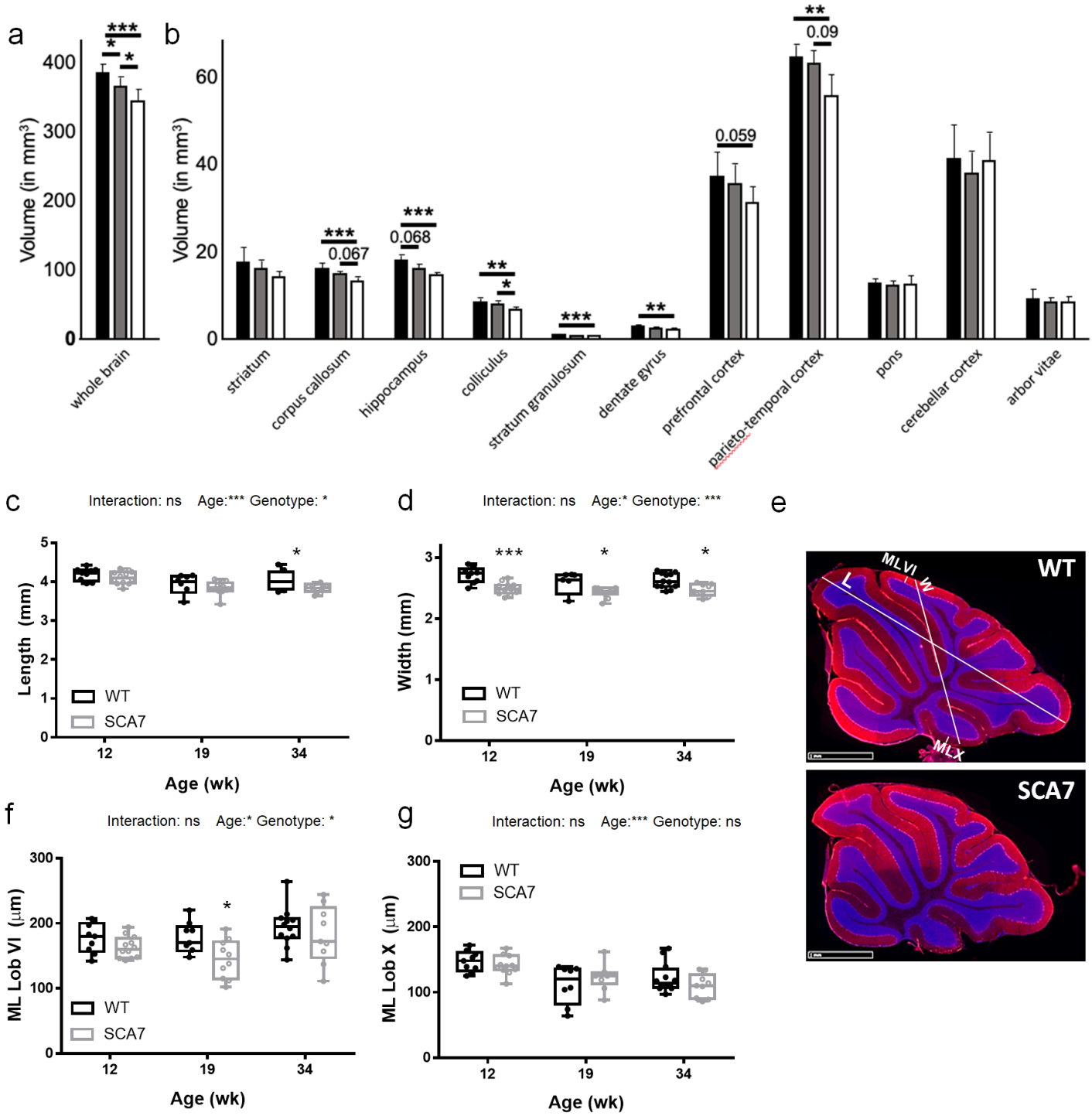

Figure 5

Brain region atrophy of SCA7 mice. a, b Ex vivo MRI measurement of whole brain volume (a) and individual brain structures (b) showing differences between wild type (WT), SCA7140Q/5Q and SCA7140Q/140Q mice at 24 weeks (black, grey and white bars, respectively); n= 8 WT, 9 SCA7140Q/5Q, 6 SCA7140Q/140Q mice. Cubic millimeter = mm3. c, d Measurement of vermis length (c) of cerebellar sections (axis from lobule V to IX in e) shows shortening at late disease stage (34 weeks (wk)) in SCA7140Q/5Q relative to WT mice, while the width (d) (axis from lobule VI to X in e) has reduced size from 12 weeks onward in SCA7140Q/5Q mice; n= 8-12 tissue sections/age-genotype. Millimeter = mm. e Representative cerebellar vermis section of WT and SCA7 mice immunolabeled with CALB1 antibody (red) and DAPI (blue). f, g Measurement of the thickness of molecular layer (ML) of lobules (Lob) VI and X of cerebellar sections shows no steady difference between SCA7140Q/5Q and WT mice; 9-12 sections/mouse Micrometer = µm. Data are expressed as mean ± SEM. Statistical analysis was performed by one-way ANOVA with post-hoc Bonferroni test (a, b) and ordinary two-way ANOVA with post-hoc Bonferroni test (c, d, f, g). * $p<0.05$, ** $p<0.01$, *** $p<0.001$. ns= not significant.

Figure 6

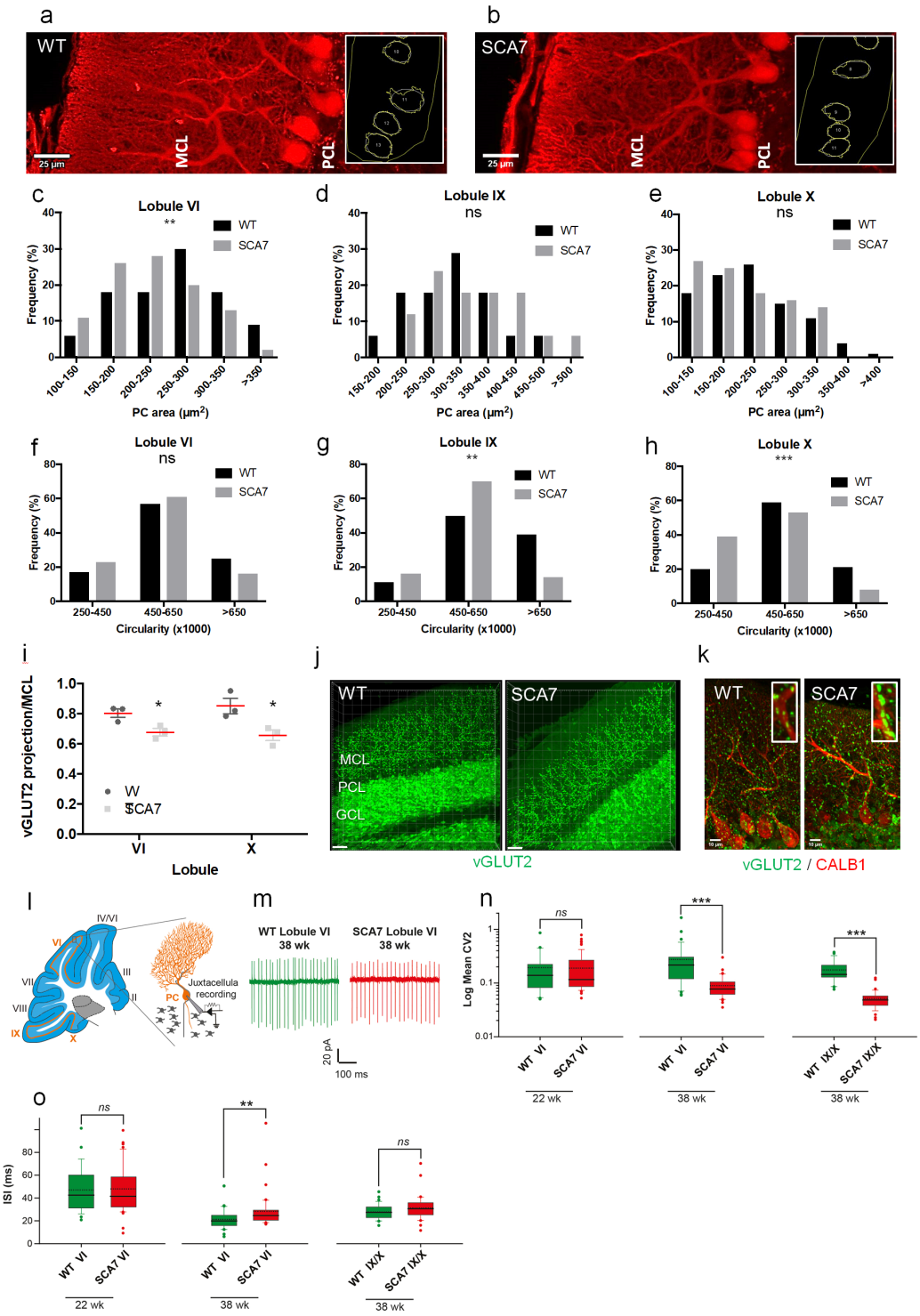

Figure 6

Alteration of morphology, synaptic contact and intrinsic activity of PCs in SCA7 mice. a, b CALB 1 immunostaining (red) of Purkinje cells (PC) in lobule VI of the vermis in wild type (WT) and SCA7 mice (left). The staining is used to evaluate the soma size and cell circularity (right). Molecular cell layer (MCL); PC layer (PCL). Scale bar = 20 µm. c-h Frequency of PC soma area (c-e) and frequency of PC circularity index (f-h) as measured in lobule VI, IX and X of the vermis of 34-week-old WT (n=3) and SCA7140Q/5Q

mice (n=3). 33-51 PC/lobule/mouse were measured. SCA7140Q/5Q mice show different distribution of PC area in lobule VI and different distribution of PC circularity in lobule IX and X, relative to WT mice. Square micrometer (µm2). i, j Width measurement of vGLUT2-labeled area in the molecular cell layer (MCL) of lobule VI and X of the vermis shows reduced width size in SCA7140Q/5Q (n=3) compared to WT mice (n=3). Data are expressed as mean ± SEM. Granular cell layer (GCL). Scale bar = 30µm. k Co-immunostaining of vGLUT2 and CALB1 showing aggregation of vGLUT2 contact points located along large dendritic arborization of PC in SCA7 cerebellum. Scale bar = 10µm. l Left: Schematic of a sagittal cerebellar section. Cerebellar lobules are numbered from I to X. Orange lines indicate the locations of PC intrinsic activity recording sites. Right: schematic of juxtacellular recording of PC pacemaking activity. m Representative traces of spontaneous firing in PCs located in lobule VI from WT or SCA7140Q/5Q mice. Week (wk). n Box-plots showing the values of CV2 of adjacent inter-spike interval (ISI) in lobule VI and IX/X in WT and SCA7 mice. Mean and median values are indicated as dashed and solid lines, respectively (22 wk old WT (n= 27) and SCA7 (n= 65); 38 wk old WT (n= 33 in lobule VI and 34 in IX/X) and SCA7 (n= 41 in lobule VI and 36 in IX/X). o Same representation as in N for ISI values. Statistical analysis was performed using Chi-square (c-h), Student t-test (i) and Mann Whitney rank-sum test (n, o). *p<0.05; **p<0.01; ***p<0.001; ns= not significant

Figure 7

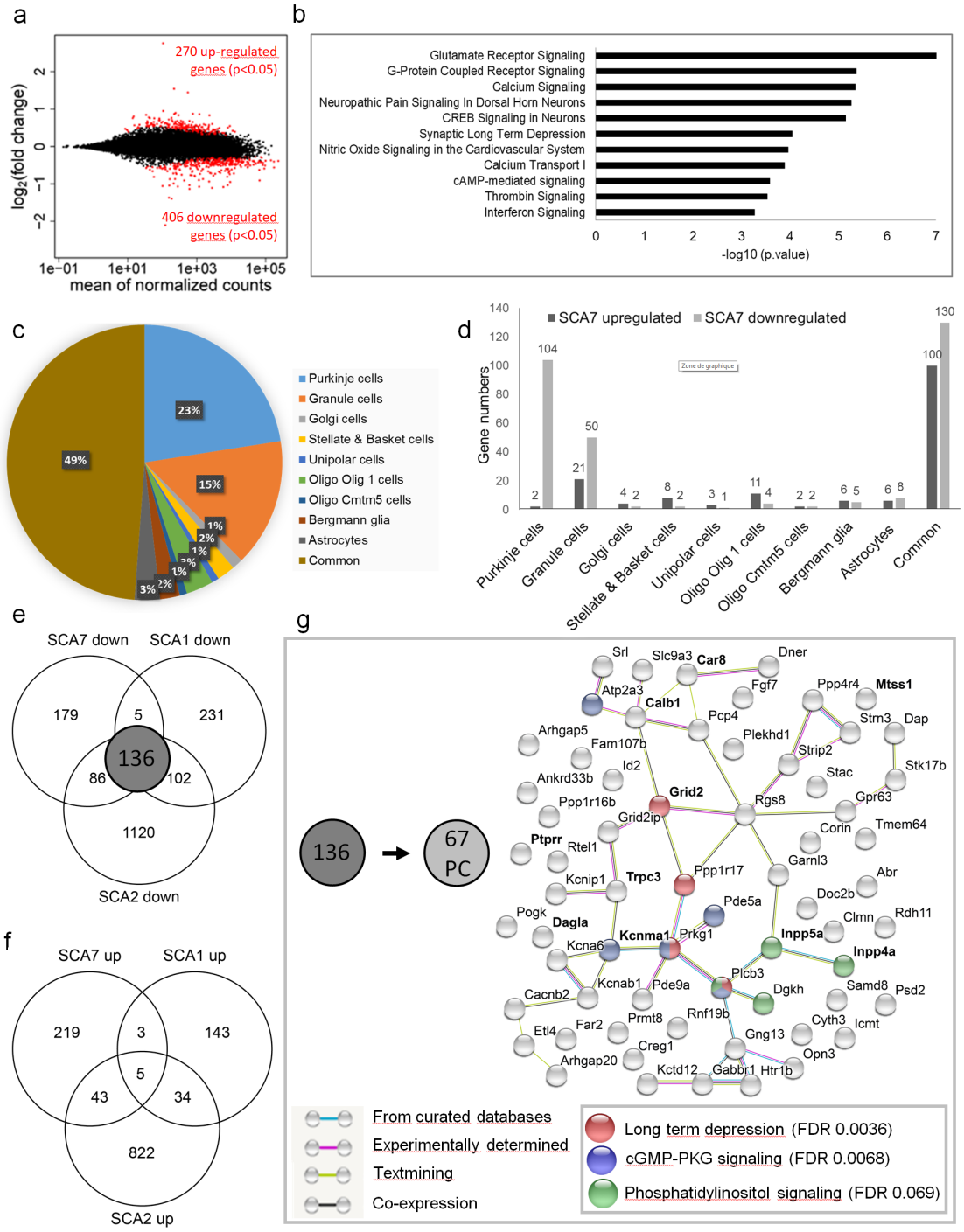

Figure 7

Gene deregulation, cell-type identity and network analysis. a MA plot of transcriptomic dataset between SCA7140Q/5Q and wild type (WT) mice cerebellum at 40 weeks of age. Red points represent 676 genes deregulated in SCA7140Q/5Q (p<0.05). b Functional annotations of the deregulated genes performed using Ingenuity Pathway Analysis. The most significantly affected pathways in SCA7140Q/5Q are indicated. c Cerebellar cell-type distribution of the genes deregulated in SCA7140Q/5Q mice based on

curated dataset of Doyle et al. (2008) [51]. d Cell-type classification of up- and downregulated genes indicates Purkinje cells as the predominant cell type affected by gene downregulation in SCA7 cerebellum. Common means genes deregulated in more than one cell type. e, f Venn diagrams showing overlap between genes downregulated (e) and upregulated (f) in SCA1 (5 week-old) [61], SCA2 (6 week-old) [60] and SCA7140Q/5Q cerebellum. g Genetic network showing functional partnerships and interactions between proteins encoded by the 67 PC-enriched genes downregulated in SCA1, SCA2 and SCA7 mouse models, as determined using the STRING software. In bold are known ataxia genes. The bottom right panel indicates functional annotations of the 67 PC-enriched genes downregulated in SCA1, SCA2 and SCA7 mouse models, using KEGG pathway analysis. False discovery rate (FDR).

Figure 8

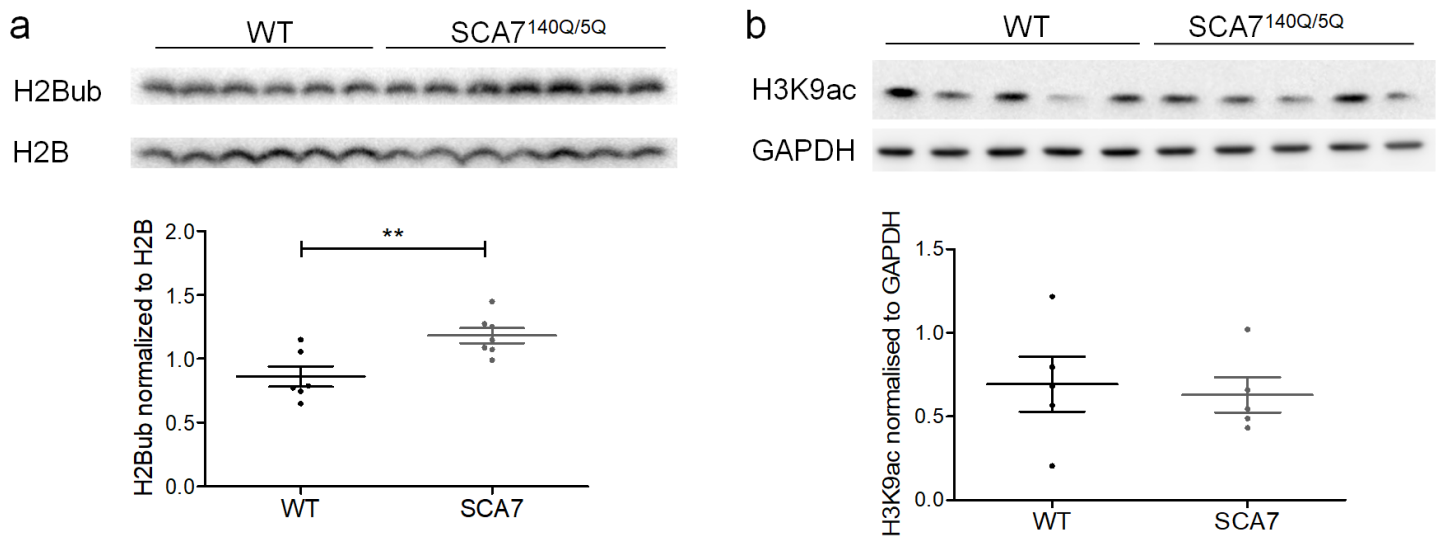

Figure 8

Alteration of SAGA-dependent histone marks in SCA7140Q/5Q cerebellum. Western blot analyses showing that (a) the bulk level of monoubiquitinated histone H2B (H2Bub) is significantly increased in the cerebellum of SCA7140Q/5Q mice compared to wild type (WT), while (b) the bulk level of acetylated lysine 9 of histone H3 (H3K9ac) is comparable in SCA7140Q/5Q and WT mice. Immunodetected signals were quantified in Fiji and normalized using the level of H2B (a) and GAPDH (b). Data represent mean ± SEM. Student's t-test, ** $p < 0$

Supplementary Files

This is a list of supplementary files associated with this preprint. Click to download.

- AllsupplFiguresS1S11.pdf
- TableS1Niewiadomskaetal.pdf

- TableS2Niewiadomskaetal.xlsx
- TableS3Niewiadomskaetal.xlsx
- TableS4Niewiadomskaetal.xlsx
- TableS5Niewiadomskaetal.xlsx
- TableS6Niewiadomskaetal.xlsx
- TableS7Niewiadomskaetal.xlsx
- TableS8Niewiadomskaetal.xlsx
- TableS9Niewiadomskaetal.xlsx
- Table.docx